PERFORMANCE ANALYSIS OF A LIQUID METAL HEAT PIPE SPACE SHUTTLE EXPERIMENT

THESIS

Timothy J. Dickinson, Captain, USAF

AFIT/GAE/ENY/96D-2

DEPARTMENT OF THE AIR FORCE
AIR UNIVERSITY
AIR FORCE INSTITUTE OF TECHNOLOGY

Wright-Patterson Air Force Base, Ohio

AFIT/GAE/ENY/96D-2

PERFORMANCE ANALYSIS OF A LIQUID METAL HEAT PIPE SPACE SHUTTLE EXPERIMENT

THESIS

Timothy J. Dickinson, Captain, USAF

AFIT/GAE/ENY/96D-2

Disclaimer Statement

The views expressed in this thesis are those of the author and do not reflect the official policy or position of the Department of Defense or the U. S. Government.

AFIT/GAE/ENY/96D-2

PERFORMANCE ANALYSIS OF A LIQUID METAL HEAT PIPE SPACE SHUTTLE EXPERIMENT

THESIS

Presented to the Faculty of the Graduate School of Engineering

of the Air Force Institute of Technology

Air Education and Training Command

In Partial Fulfillment of the

Requirements for the Degree of

Master of Science in Aeronautical Engineering

Timothy J. Dickinson, B.S.A.E.

Captain, USAF

December 1996

Acknowledgments

I am greatly indebted to my thesis advisor, Lt Col W. Jerry Bowman, for his guidance and heat pipe expertise. His focus on critical aspects of the analysis maximized the benefits of this research. An exemplary supervisor, he ensured my personal success and the technical success of this study. I also appreciate the efforts of Maj Little and Dr. King to improve the presentation of this material.

This research program was sponsored by Mr. Marko Stoyanof of the Air Force's Phillips Laboratory. He provided travel funds and assembled a team of engineers from Phillips Laboratory and the DoD Space Test Program to support the mission. His tireless efforts and those of Mr. Dave Glaister, Lt Jon Anderson, Capt Brad Tabor, and Mr. Tom Stuart resulted in round-the-clock operation for more than 200 hours. The DoD Space Test Program also funded payload integration and NASA mission support.

I am especially grateful to Mr. Keith Woloshun, Mr. Mike Merrigan, and Mr. Tom Sena of Los Alamos National Laboratory. They educated me on the design and manufacture of heat pipes and assisted in data analysis. Most significantly, the three excellent heat pipes built by their team were critical to the success of this effort.

I commend Mr. Charles McNeely for retrieval of the corrupted thermal vacuum data. Without his help, the ground data and much science would have been lost. The lab technicians should be commended for their outstanding support in general.

Finally, I want to thank my wife, Lanna, for her support during the long hours and short weekends. Her continual patience and encouragement are deeply appreciated.

Timothy J. Dickinson

Table of Contents

List of Figures

List of Tables

List of Symbols

Roman Letters

A_v	vapor passage cross sectional area (m^2)
A_w	working fluid cross sectional area (m^2)
C	heat capacity per unit length of wall, wick, and working fluid (J/mK)
D_v	vapor passage diameter (m)
d	effective molecular diameter of working fluid (m)
F_l	liquid friction coefficient (N/m^3W)
F_v	vapor friction coefficient (N/m^3W)
h_{fg}	latent heat of vaporization (J/kg)
K´	ratio of constant pressure and constant volume specific heats
Kn	Knudsen number
k_{eff}	effective thermal conductivity of wick and working fluid (W/mK)
L_{eff}	effective heat pipe length (m)
L_{evap}	evaporator length (m)
p_v	vapor pressure (N/m^2)
p_0	vapor pressure at evaporator end cap (N/m^2)
Q	heat transfer rate (W)
R	heat pipe thermal resistance (K/W or °C/W)
R_g	gas constant (J/kgK)

r_{eff} effective wick pore radius (m)

r_{hyd} hydraulic wick pore radius (m)

r_i wall inner radius (m)

ΔT_{crit} superheat required for boiling (K or °C)

T_{cond} average condenser temperature (K or °C)

T_{evap} average evaporator temperature (K or °C)

T_{melt} working fluid melt temperature (K or °C)

T_0 vapor temperature at evaporator end cap (K or °C)

T_∞ temperature of surroundings (K or °C)

Greek Letters

η heater efficiency

κ Boltzmann constant (J/K)

μ dynamic viscosity (kg/ms)

ρ_l liquid density (kg/m^3)

ρ_v vapor density (kg/m^3)

ρ_0 vapor density at evaporator end cap (kg/m^3)

σ coefficient of surface tension (N/m)

ϕ wick porosity

Abstract

Future spacecraft technologies require advanced high-temperature thermal control systems. Liquid metal heat pipes are considered ideally suited for such applications. However, their behavior during microgravity operation is not yet understood. This study investigated liquid metal heat pipe performance in such an environment. Three stainless steel / potassium heat pipes were flown on space shuttle mission STS-77 in May 1996. The objectives of the experiment were characterization of the frozen startup and restart transients, comparison of flight and ground test data to establish a performance baseline for analytical model validation, and assessment of three different heat pipe designs.

Heat pipe performance was characterized prior to the flight experiment. Predicted performance envelopes for each heat pipe were determined from theoretical calculations. Performance baselines were established from ground thermal vacuum test results. These pre-flight results were compared with those from the flight experiment. Thermal resistances were calculated for comparison of each heat pipe design.

Microgravity operation did not adversely impact the startup or restart behavior of the heat pipes. The heat pipes operated within the predicted performance envelopes. The three designs had distinct startup characteristics yet similar steady-state performance. These results will serve as a benchmark for further liquid metal heat pipe studies and space system applications.

PERFORMANCE ANALYSIS OF A LIQUID METAL HEAT PIPE SPACE SHUTTLE EXPERIMENT

I. Introduction

Problem Statement

Performance characteristics of liquid metal heat pipes are not established for microgravity operation. Model analyses and ground tests predict the performance of these heat pipes but the results have not been verified by microgravity tests. Ground tests reveal startup from the frozen state as the critical phase of operation since condensed liquid may freeze in the condenser and lead to evaporator dryout. In terrestrial applications, gravity can assist in the return of condensed fluid to the evaporator when the evaporator is positioned below the condenser, thus minimizing dryout risk. Space systems, however, do not have this advantage and it has been assumed until now that startup may prove a significant challenge since liquid flow relies solely upon the capillary pumping ability of the wick. The simulation of a microgravity environment or prediction of its effects is difficult to achieve on earth. Therefore, flight tests in low earth orbit are essential to adequately quantify the performance of liquid metal heat pipes in this unique environment (1; 2; 3; 4:277-278).

Importance of Research

Heat pipes have been utilized as efficient thermal control devices in space systems since 1968 (5:17). Current systems operate in the -200 °C to 200 °C temperature range

(6:21,42-43); future applications must operate in excess of 250 °C (3). Liquid metal heat pipes are specifically designed for these high temperatures. They are proven performers in terrestrial applications and have advantages over current spacecraft thermal control technologies. However, engineering confidence is vital to the incorporation of these devices into future thermal control systems (1).

The applications for liquid metal heat pipes include advanced military and commercial systems for spacecraft energy storage, energy generation, and electronic communications. Sodium sulfur batteries are in development at the U.S. Air Force's Phillips Laboratory and offer the potential for increased power density and significantly reduced mass compared to conventional spacecraft batteries. Their operation at temperatures in excess of 250 °C requires unique thermal management approaches; these approaches could include liquid metal heat pipes. Advanced solar concentrators, in development at the National Aeronautics and Space Administration (NASA) and Phillips Laboratory, will increase the efficiency of power generation and electric propulsion systems. One prototype system will operate at 300 °C and could utilize liquid metal heat pipes to transport and distribute thermal energy. Liquid metal heat pipe technology may also assist satellite contractors in the development of advanced communication electronics (3; 7:339).

Liquid metal heat pipes offer advantages over current spacecraft thermal control systems. Power generation and conversion systems, notably nuclear reactors and thermionic devices, can realize improved energy transport efficiencies with high temperature heat pipes (8). These heat pipes may also play a role in the replacement of

radioisotope thermoelectric generators; one concept retains the isotope power source and employs heat pipes to transfer energy to a conversion system. Heat pipes can also transport thermal energy from rocket nozzle throats. This application reduces the weight, expense, and complexity of ablative and regenerative cooling systems. In the same manner, liquid metal heat pipes can function as radiators to transfer excess thermal energy to space (8; 9).

Research Objectives

This investigation responds to the requirements of various organizations within the Department of Defense, NASA and industry. Three research objectives were established to meet these requirements:

1) Characterize the frozen startup and restart behavior of liquid metal heat pipes in a microgravity environment

2) Compare microgravity and ground test results to establish a performance baseline for future analytical model validation

3) Assess the performance of three heat pipe designs

Liquid metal heat pipe behavior in a microgravity environment is not well understood (2). Heat pipe scientists and engineers require microgravity performance data to provide this knowledge and benchmark analytical models (10:242). Achievement of the first two objectives will meet this requirement. Numerous wick designs exist for liquid metal heat pipes. The optimum structures for microgravity operation are unknown (2). Fulfillment of the third objective provides this necessary information to heat pipe designers. The following section details the research approach for attainment of these objectives.

Methodology

Historical Synopsis. Three stainless steel / potassium heat pipes were designed, manufactured, integrated and recently tested during a space shuttle mission. This research program was sponsored by Phillips Laboratory and conducted from 1991 to 1996.

Los Alamos National Laboratory was awarded a contract for the design and manufacture of the heat pipes in 1991; fabrication is discussed in detail in Chapter Two. The experiment was accepted as a shuttle payload the following year. The heat pipes were delivered to Phillips Laboratory in 1993 for integration and pre-flight characterization tests. The platform was integrated during 1994 and underwent thermal vacuum tests at Sandia National Laboratory in 1995; ground tests are detailed in Chapter Three. The experimental platform was then shipped to NASA for payload integration and final interface verification. The experiment, designated the Liquid Metal Thermal Experiment, was flown on space shuttle mission STS-77, 19-28 May 1996. Funds for shuttle integration and mission support were provided by the Department of Defense Space Test Program (3).

Research Approach. The author provided technical support for the mission and conducted post-mission analysis. A three-phase approach provided the required support and achieved the technical objectives:

1) Collect flight experimental data
2) Analyze ground and flight test results
3) Document and present conclusions

These phases, conducted between May and November 1996, are discussed below.

The first phase involved support of the ten day space shuttle mission. Three teams of engineers conducted tests continuously for nine days; this resulted in 200 hours of test data. Changes to the test plan were recommended by the author to ensure achievement of the objectives and enhance the technical merit of the experiment. Data reduction and analysis during the mission supported these changes.

Analyses of the flight and ground data in the second phase addressed the three technical objectives outlined earlier. Flight data consisted of heat pipe wall temperature measurements as a function of time for various test scenarios. These scenarios, discussed in detail in Chapter Four, addressed all three objectives. Ground data included ground thermal vacuum test results and theoretical calculations of heat pipe performance envelopes; these efforts supported the second and third objectives respectively.

Experimental results were communicated to heat pipe specialists in the final phase. Submission and defense of this thesis marked the beginning of the phase. This study was also documented in a Phillips Laboratory technical report. Experimental data and results will be submitted for publication and presented at one or more technical conferences in 1997.

Review of Heat Pipes

Heat Pipe Operating Principles. A heat pipe transports thermal energy efficiently and effectively. It consists of a porous capillary wick structure and working fluid enclosed in a container. The container is divided into three sections: evaporator, adiabatic and condenser. The working fluid vaporizes in the evaporator when energy is extracted from a heat source. The vapor flows through the adiabatic section to the

condenser where it condenses and releases the latent heat of vaporization to a heat sink. The capillary pressure of the wick returns the condensed fluid to the evaporator to complete the cycle. This process is depicted in Figure 1. This transport of energy can occur at a high rate, over a considerable distance, and with an extremely small temperature drop. Along with the advantages of simple construction and operation, a heat pipe is highly accessible to control and does not require any external pumping power (11:1).

Three Types of Heat Pipes. Cryogenic heat pipes operate at temperatures below -150 °C and are used in communication and defense satellites to cool infrared sensors and lasers. Examples of cryogenic working fluids are nitrogen and oxygen. Moderate-temperature heat pipes are perhaps the most common; they cool electronics, machinery, and spacecraft as well as transport heat in energy recovery and conversion systems. They use fluids such as water, ammonia, and freon and operate in the temperature range

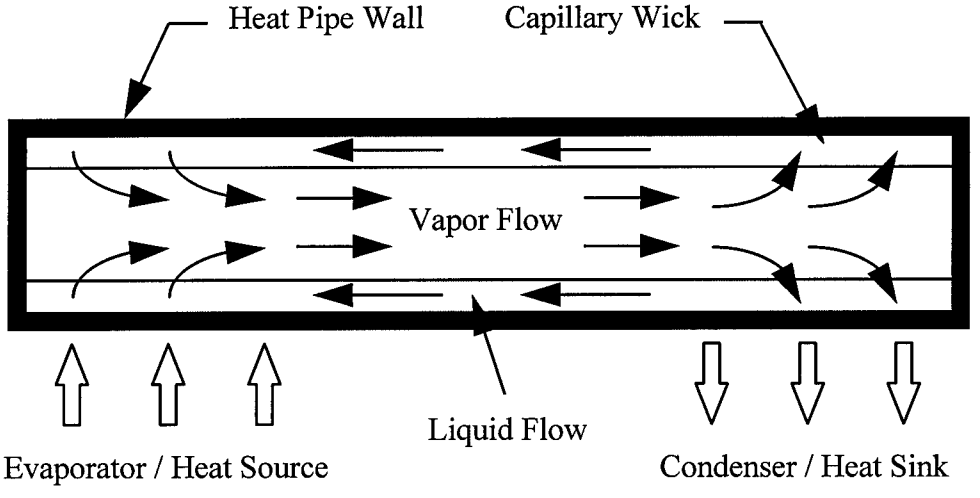

Figure 1 : Heat Pipe Operation

between cryogenic and liquid metal heat pipes. Liquid metal heat pipes operate above 250 °C in nuclear reactors, thermoelectric generators, and gasification plants. Common working fluids are sodium, potassium and lithium (11:3-5,14-29).

Phases of Operation. Silverstein (12:249-251) describes three phases of operation for heat pipes: non-operational, startup and operational. These three phases are described below for a liquid metal heat pipe initially at ambient temperature with the working fluid in the frozen state.

The non-operational phase begins with initiation of the startup transient and continues until continuum flow is established in the evaporator. While the heat pipe is at ambient temperature, energy is applied to the evaporator. Heat is conducted through the wall and wick and melts the frozen fluid in the evaporator. As the fluid melts, evaporation occurs at the liquid-vapor interface. Initially, the vapor flow is in a rarefied condition due to the low vapor pressure of liquid metals. Vapor accumulation continues in the evaporator and the vapor pressure increases until it becomes sufficient to produce continuum flow. A front exists between vapor in the rarefied and continuum conditions and its location is evidenced by a sharp temperature gradient. Continuum flow must be established for vapor propagation along the heat pipe.

The startup phase begins after the establishment of continuum flow throughout the evaporator. During the startup phase, the continuum front advances axially along the heat pipe. Minimal heat transfer occurs beyond the continuum front due to the low density of rarefied vapor. The continuum front therefore divides the heat pipe into active and inactive regions. A portion of the heat pipe is inactive during startup and at low

operating temperatures. Stabilization of the front or its arrival at the end of the condenser indicates conclusion of the startup phase. Excellent figures describing the startup process of liquid metal heat pipes are provided in Faghri's text (6:313).

The heat pipe enters the operational phase upon startup completion. The heat pipe becomes nearly isothermal after arrival of the continuum front at the condenser end cap. The heat pipe temperature will remain nearly isothermal and continue to rise until a steady-state condition is reached. Any future change in the heat input rate will cause a response in heat pipe temperature.

Heat pipe performance during these phases is constrained by various heat transfer limitations. The limitations applicable to liquid metal heat pipes are described in Chapter Three.

Gravity can affect heat pipe operation during the startup and operational phases. If the evaporator is positioned below the condenser, gravity will assist capillary forces in the return of condensed fluid to the evaporator. In the same manner, gravity can also oppose capillary forces if the relative positions are reversed. Heat pipe operation in a horizontal position negates such effects. However, even in a horizontal position, gravity could alter the circumferential distribution of working fluid in the wick and result in pooling along the bottom of the heat pipe. Gravity could thus result in an uneven distribution of working fluid in the frozen state.

Review of Microgravity Heat Pipe Experiments

Cryogenic and moderate-temperature heat pipes have been tested in microgravity environments for almost 30 years. Test beds include sounding rockets, satellites, and the

space shuttle. Microgravity tests of liquid metal heat pipes had not been accomplished prior to this investigation.

Cryogenic Heat Pipes. Cryogenic heat pipe experiments were flown on two space shuttle missions. The first test occurred on shuttle mission STS-53 in 1992. Two oxygen heat pipes demonstrated the ability to start from super critical temperatures and operate in the range of -210 °C to -130 °C (13). In 1994, another experiment was flown on STS-62 (14). A nitrogen heat pipe, containing five copper cable wicks, failed to start after two attempts; failure was attributed to excessive nitrogen.

Moderate-temperature Heat Pipes. The first heat pipe flown in space was constructed of stainless steel and used water as the working fluid. It was orbited in 1967 by an Atlas-Agena vehicle. The heat pipe successfully demonstrated normal heat pipe operation in a microgravity environment. Aluminum alloy / freon heat pipes were tested the following year on the GEOS-B satellite. These heat pipes were the first to provide satellite thermal control (5:17).

At least eight moderate-temperature heat pipe experiments were flown in the 1970s. Successful startup under adverse conditions and operation at large heat loads were demonstrated. Three of the eight were flown on sounding rockets; the rockets provided six to eight minutes of microgravity test time. The other five were flown on satellites; the satellites provided test times from several months to more than six years (7:318-329).

The sophistication of microgravity experiments increased in the 1980s and 90s with the use of the Long Duration Exposure Facility (LDEF) and space shuttle. Two

heat pipe experiments on the LDEF and one on shuttle mission STS-8 examined space radiator applications (7:325; 15). An experiment flown on STS-52 in 1992 determined the performance limits of two aluminum / freon heat pipes under applied acceleration (16). A capillary pumped loop experiment, flown on STS-69, demonstrated startup under difficult conditions and robustness during stressful operations (17).

Review of Liquid Metal Heat Pipe Research

Analytical Models. The wide interest in liquid metal heat pipes has stimulated the development of numerous analytical models. Hall and Tournier have produced the most complex and thorough models. Both models simulate liquid-vapor counter flow and include hydrodynamic coupling at the liquid-vapor interface. Hall and his co-workers (18; 19) developed the THROHPUT (Thermal Hydraulic Response Of Heat Pipes Under Transients) code to examine startup and shutdown of liquid metal heat pipes. Tournier and El-Genk (20) developed a two-dimensional transient analysis code to model liquid metal heat pipe operation. Their model also addresses phase change of the working fluid and rarefied vapor flow during startup. These models provide the most detailed, accurate, and efficient analysis of the startup of liquid metal heat pipes from the frozen state. This investigation provides the first opportunity to benchmark these models with microgravity performance data.

Experiments. Experimental work has focused on the characterization of startup, steady-state, and shutdown operations of liquid metal heat pipes. Extensive studies conducted at Los Alamos National Laboratory (21; 22; 23; 24; 25) have established a database for performance of terrestrial systems. Prototype heat pipe designs for space

applications have been tested in simulated environments. These applications include thermal management of reentry vehicle leading edges (26) and solar power receiver systems (27). However, microgravity effects were ignored in these tests. This investigation addresses such effects.

During the 1980s, a space nuclear reactor with liquid metal heat pipes was designed and built for flight tests by the Air Force Weapons Laboratory (presently Phillips Laboratory) at Kirtland AFB, NM. Thermal energy was transferred from the reactor core by 120 molybdenum alloy / lithium heat pipes. Unfortunately, the SP-100 Heat Pipe Space Nuclear Reactor System (9:1-22) was canceled before flight tests could be conducted. This program was the first to pursue microgravity tests of liquid metal heat pipes.

Thesis Overview

This thesis presents the data and analyses of a liquid metal heat pipe space shuttle experiment. This chapter introduces the problem, discusses the importance and approach of the research effort, and provides a background on liquid metal heat pipes. Chapter Two addresses the design and fabrication of the experimental platform and Chapter Three discusses pre-flight characterization of the heat pipes. Chapter Four presents the flight test scenarios, procedures, and environment. Chapter Five details analyses of the flight and ground experimental data. The conclusions and recommendations offered in the final chapter provide government and industry with information critical to the advancement of spacecraft thermal control technology.

II. Experimental Setup

Introduction

This chapter describes the design, fabrication, verification, and integration of the experimental platform. Los Alamos National Laboratory designed and fabricated the heat pipes under a Phillips Laboratory contract. Phillips Laboratory and various organizations verified and integrated the hardware. NASA conducted final integration and pre-flight checkout at Kennedy Space Center.

Design

General design parameters of the heat pipe components are described below. Detailed specifications and material physical properties are provided in Tables 1 and 2 located in Appendices A and B respectively.

Containers. The heat pipe containers were constructed of Type 304 stainless steel. Each heat pipe had the same external dimensions: 61.0 cm length, 2.30 cm outside diameter, and 0.089 cm wall thickness. The length was divided into a 8.9 cm evaporator and a 52.1 cm condenser; an adiabatic section was not present (28).

Wick Structures. The wicks were constructed of Type 304 stainless steel as well. The three wick structures were homogeneous, annular gap, and arterial and are illustrated in Figure 2 (28). These designs were chosen due to their characteristic differences; these differences are discussed below. Ideally, a heat pipe wick should have high capillary pumping ability, thermal conductivity, and permeability (6:27).

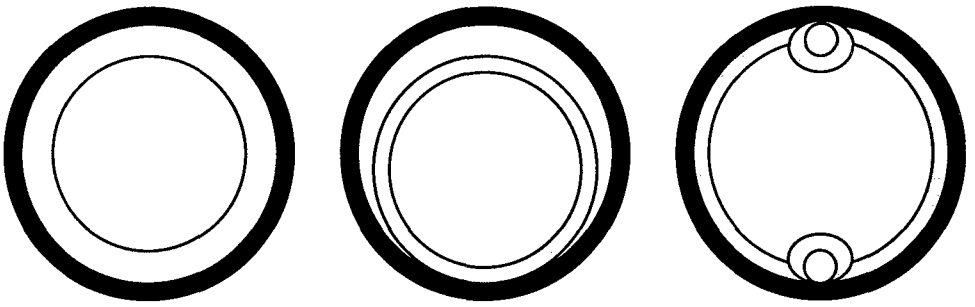

Homogeneous Annular Gap Arterial

Figure 2 : Wick Structure Designs

All three wick designs have a high effective thermal conductivity since the working fluid is a liquid metal. The homogeneous wick structure is a simple, classic design and serves as an ideal baseline for comparison against the other designs. It excels in capillary pumping ability due to the fine pores at the wick surface but offers low permeability. The annular gap wick retains favorable capillary pumping ability but also provides increased permeability due to the unimpeded flow path for condensed fluid. However, annular gap wick designs may encounter priming difficulties during startup. The arterial wick structure also combines high capillary pumping ability and high permeability. The disadvantage of this structure is the potential for vapor bubble formation in the arteries during startup; vapor bubbles are difficult to collapse and may prevent the return of condensed liquid (6:25-31).

The homogeneous wick was composed of 11 layers of 100 mesh screen and was 0.23 cm thick. The annular gap and arterial wicks were composed of 4 layers of 250 mesh screen and were 0.03 cm thick. The annular gap wick had a 0.10 cm annulus; the

annulus is defined as the maximum distance between the wick and container wall. The arterial wick had two 0.10 cm diameter arteries positioned 180° apart (28).

Working Fluid. Each of the heat pipes was charged with potassium. At atmospheric pressure, potassium melts at 64 °C and boils at 759 °C (6:21). The intended amount of working fluid allows complete saturation of the wick during operation and provides a 2.0 cm pool of reserve liquid in the condenser to protect against evaporator dryout. Based on these two conditions, the homogeneous, annular gap, and arterial wicks required 44.0, 42.7, and 17.3 grams of potassium respectively (28).

Fabrication

Components. Los Alamos National Laboratory fabricated and individually cleaned all heat pipe components prior to assembly. A stainless steel tube with a 2.54 cm outside diameter and 0.089 cm thickness was cut into three 76.0 cm long sections to form the heat pipe containers. The heat pipe end plugs and fill tubes were also fabricated from stainless steel. Mesh screens were cut to the appropriate length for the wicks. Wick mandrels were fabricated from copper tubing. All components, including the mandrels, were cleaned according to the procedure outlined in Appendix C (29).

Wick Structures. The screens were wrapped around the mandrels, as shown in Figure 3, to form the wick structures. The wicks and mandrels were inserted into the containers. These assemblies were drawn down to achieve 20% compression of the wicks and the final outside pipe diameter of 2.30 cm. The pipes were cut to a length of

Figure 3 : Wick Fabrication

61.0 cm and the copper mandrels were dissolved with acid. The wicks were removed, sintered, and returned to the containers. The end plugs and fill tubes were welded to the containers to complete structural assembly. These procedures are described in detail in Appendix C (29).

Working Fluid. Each heat pipe was charged with potassium after a leak check and vacuum degas of the container and wick. A container of known volume was filled with liquid potassium; each heat pipe required a different amount of working fluid and therefore had its own volume pot. The potassium was transferred from the volume pot into a distillation pot. The distillation pot was connected to a vacuum line and the heat pipe to form the distillation apparatus. This apparatus allowed the distillation of the potassium while it was transferred to the heat pipe. The fill tube was cut and sealed after

completion of the potassium charge. A detailed description of these procedures is found in Appendix C (29).

The amounts of potassium distilled into the heat pipes were 46.0, 61.5, and 19.2 grams for the homogeneous, annular gap, and arterial wick designs respectively. This represents an overcharge for each heat pipe. In general, it is more favorable to overcharge than to undercharge, since an undercharge can lead to evaporator dryout. The homogeneous and arterial wick heat pipes were overcharged by 4.5% and 11.0%, an insignificant excess with regard to operational effectiveness. The annular gap wick heat pipe, however, received a significant 44.0% excess (29).

Verification

Leak Check and Weld Inspection. A leak check was performed on the individual heat pipes at Los Alamos National Laboratory prior to delivery to Phillips Laboratory (29). Phillips Laboratory conducted a leak check on the final flight configuration after completion of thermal vacuum, random vibration, and pressure proof tests. In both cases, no potassium or evidence of reaction was found. Weld integrity was certified by OAO Corporation through radiographic inspection (30). The inspections were conducted according to MIL-STD-2219 Class A and MIL-STD-453C Level 1.

Structural Analyses. Initial structural analyses were conducted by The Aerospace Corporation. Their examination of the static, buckling, thermal, and modal behavior of the integrated platform revealed positive margins of safety for all conditions (30).

Vibration Test. CSA Engineering, Incorporated validated the integrated platform at flight qualification levels in a random vibration test. The lowest vibrational mode occurred at 82 Hz, above the minimum threshold of 50 Hz (30).

Pressure Proof Test. OAO Corporation subjected the heat pipes to a pressure proof test at 658 °C for one hour. At this temperature, the saturation vapor pressure of potassium is twice that at 600 °C, the maximum expected temperature during ground and flight tests. All dimensional changes were within the maximum allowable 0.2% (30).

Thermal Proof Test. Los Alamos National Laboratory tested the heat pipes individually in a vacuum chamber prior to delivery. The chamber is shown in Figure 4. Each pipe experienced two startup and shutdown cycles. A 350 W step input was applied to the evaporator by a radio frequency induction heater and heat removal was continuously monitored with a water-cooled calorimeter. The temperature profiles were consistent with heat pipe startup theory (1).

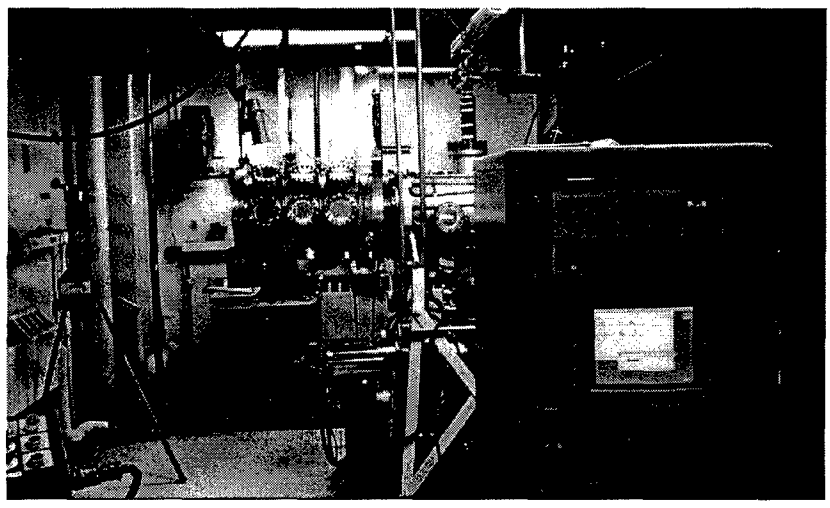

Figure 4 : Thermal Proof Test at Los Alamos National Laboratory

Phillips Laboratory also conducted thermal proof tests of the individual heat pipes prior to integration and thermal vacuum tests. The pipes were operated horizontally in a vacuum chamber. A resistance heater coupled to the evaporator provided stepped power increments up to 304 W. The heat transfer environment was confined to radiation exchange between the heat pipe and test chamber; the walls of the chamber were maintained at room temperature. The temperature profiles were similar to the Los Alamos test results (31).

Integration

Support Frame. The aluminum experimental support frame consisted of two 50.0 cm diameter end plates connected by a 71.0 cm long center divider plate. The center divider plate separated the platform into two volumes. One volume contained the heat pipes and the other housed the experimental control unit. A stainless steel reflector plate was mounted to the heat pipe side of the divider plate; the plates were separated by 1.25 cm ceramic spacers. The reflector plate provided insulation for the electronics and support for the thermocouple wire channels. An aluminum mounting plate was positioned 3.25 cm from the other side of the center divider plate. The experimental control unit was attached to the mounting plate (2; 30). The integrated experimental platform is pictured in Figure 5.

Heat Pipes. The mounting flange of each heat pipe, attached to the evaporator end cap, was cantilevered to the top end plate of the support frame. Ceramic spacers

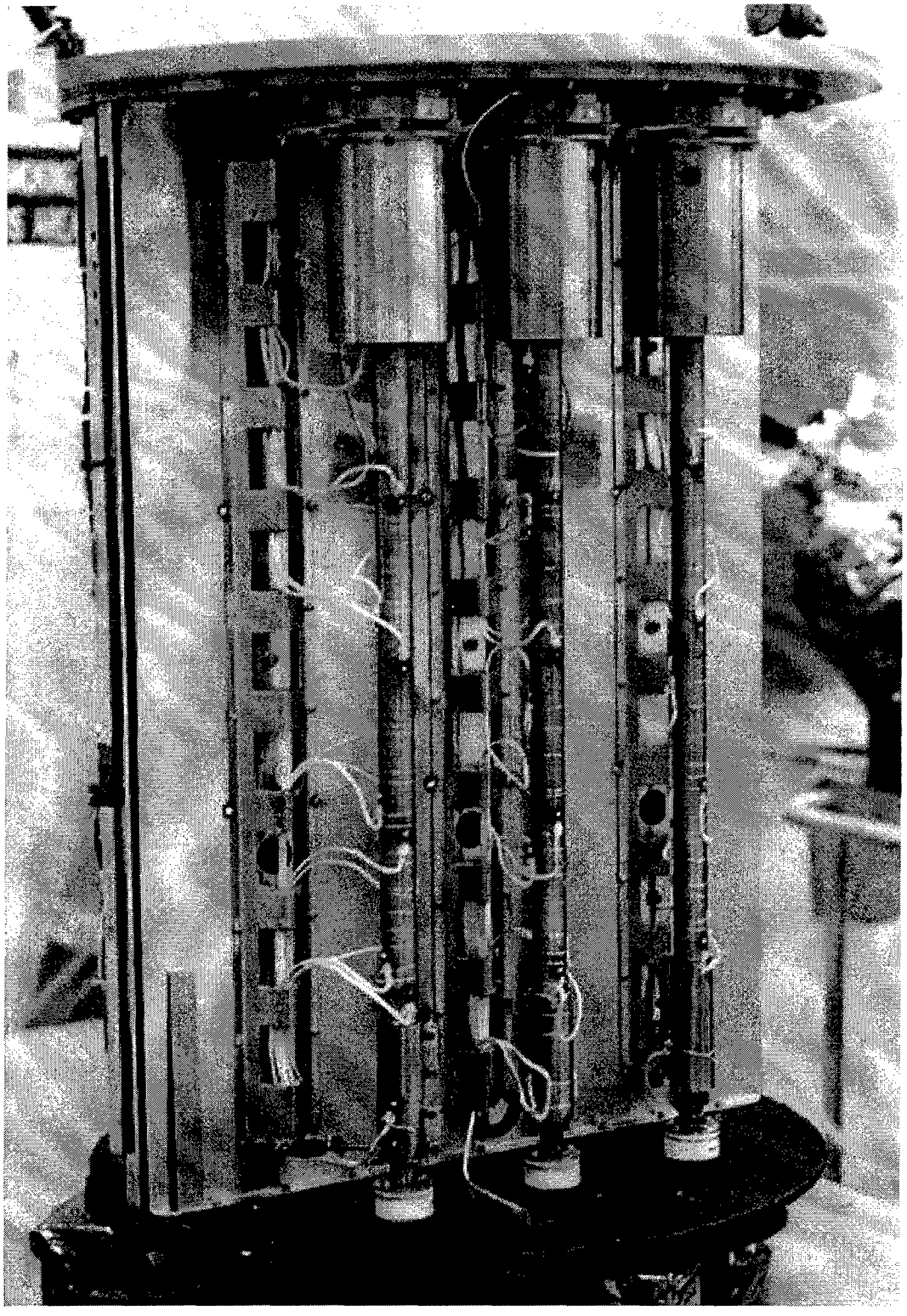

Figure 5 : Experimental Platform

insulated the top end plate from the heat pipes. The condenser end caps were secured to the bottom end plate with ceramic glass sockets. The sockets provided insulation, prevented lateral motion, and allowed axial expansion and contraction of the pipes (30).

Heaters. Helical nichrome resistance heaters were attached to the evaporator and condenser of each heat pipe. The evaporator heaters provided primary power input during the tests. The condenser heaters were intended for contingency operations; they could melt frozen potassium in the condenser section and thus assist evaporator dryout recoveries. Thin stainless steel jackets held the heaters flush with the heat pipe end caps and ensured contact during thermal expansion and contraction. The heaters had a radial thickness of 0.4 cm and the lengths were 8.9 cm and 7.6 cm for the evaporator and condenser respectively (2; 30). The heaters and jackets are shown in Figure 6.

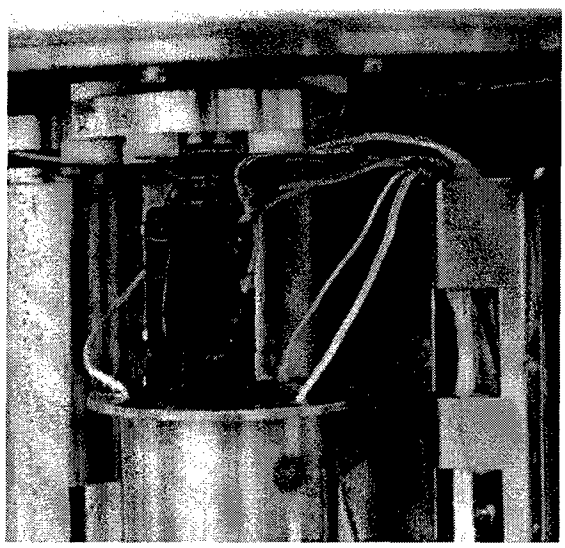

Evaporator Heater with Jacket

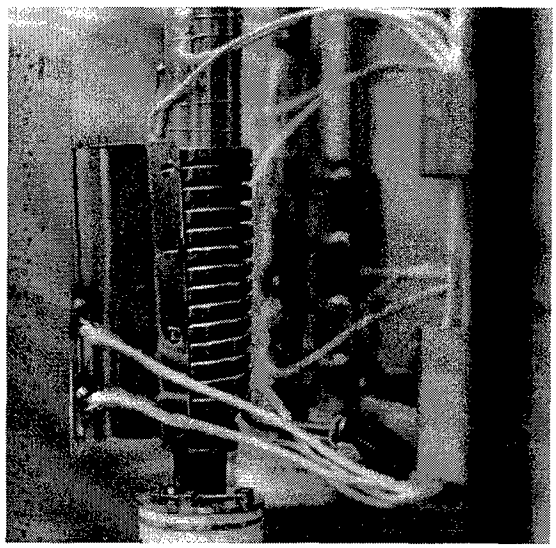

Condenser Heater with Jacket Removed

Figure 6 : Heat Pipe Heaters

Evaporator Enclosures. The evaporator end of each heat pipe was inserted into a stainless steel cylindrical enclosure. The enclosure was 7.6 cm in diameter and extended 11.1 cm from the evaporator end cap. One end was cantilevered to the top end plate of the support frame; the heat pipe passed through a 3.8 cm diameter hole in the other end. Radiation loses from the evaporator heater were minimized with seven layers of molybdenum shielding. A sheet of molybdenum was rolled into a coil and insulated thermocouple wire formed a spacer between each layer. The coil was inserted inside the cylindrical enclosure. Conductive loses from the enclosure were minimized with ceramics spacers between the enclosure and top end plate (2; 30).

Instrumentation. Component temperatures were obtained with Type K thermocouples during ground thermal vacuum and flight tests. Heat pipe temperatures were monitored with twenty-four thermocouples: sixteen along the condenser between the evaporator enclosure and condenser heater and four on each evaporator and condenser heater jacket. The thermocouples along the condenser were spaced 2.5 cm apart and rotated 90° with respect to the previous one. Their locations are provided in Table 3 and Figure 22 in Appendix D. Environment temperatures were observed with three thermocouples welded between each evaporator enclosure and molybdenum insulation shield, two on the reflector plate, and one on each support frame end plate. The experimental control unit was monitored with eight thermocouples. All thermocouple wires were routed to the experimental control unit (30).

Experimental Control Unit. The main components of the experimental control unit were the flight computer, experiment harness, power converters, and voltage

regulators. A space-qualified SC-4 computer manufactured by Southwest Research Institute controlled test cycles, processed commands from the payload ground support equipment, and transferred data to the ground through telemetry. The experiment harness provided the power and control interface with the shuttle avionics. Power converters and voltage regulators maintained a constant 28 volt power supply to the payload and the appropriate heater power during tests (30).

Hitchhiker Flight Canister and Bridge. The 59 kg experimental platform was installed in a NASA Hitchhiker flight canister. The uninsulated canister provided maximum heat rejection from the payload. The white painted exterior had an emissivity of 0.86 while the black interior had an emissivity of 0.80. A butterfly vent valve, located on the canister bottom plate, opened on orbit to achieve the required 10^{-4} torr vacuum. The canister was mated to the Hitchhiker bridge prior to integration with the orbiter Endeavour. The position of the canister and bridge are indicated in Figure 7. Final interface checkout occurred one day prior to launch (2; 30).

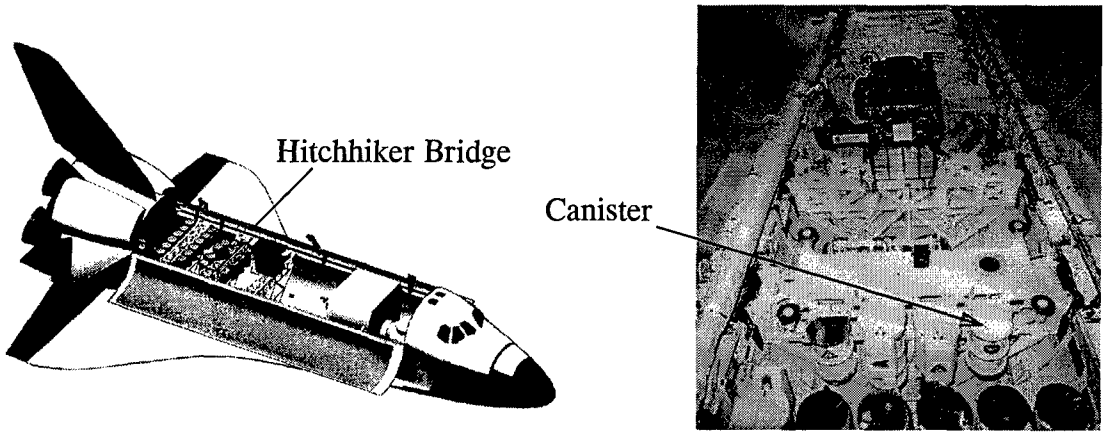

Figure 7 : Space Shuttle Payload Bay

Summary

The design, fabrication, and initial verification activities occurred at Los Alamos National Laboratory between 1991 and 1993. Further verification was accomplished by Phillips Laboratory and their supporting organizations. Numerous tests of the individual heat pipes and integrated platform certified the design and fabrication as well as demonstrated appropriate heat pipe performance. Integration began after individual heat pipe verification and was completed in early 1996 at NASA's Kennedy Space Center. The payload was approved and flown on space shuttle mission STS-77, 19-28 May 1996.

III. Pre-flight Characterization

Introduction

Heat pipe performance was predicted through two efforts. The first effort was accomplished by the author and focused on analytical calculation of the heat pipe performance envelopes. The second effort was a set of ground thermal vacuum tests conducted by Phillips Laboratory prior to the flight experiment. These tests established a performance baseline. Both efforts and their results are described below.

Performance Envelopes

Faghri (6:32-34,221-222) discusses seven heat transfer limitations applicable to liquid metal heat pipes. Six of these limits are classical limitations. Three of the six are commonly encountered during heat pipe startup but do not represent operational failure: vapor continuum, viscous, and sonic limits. The other three, however, represent failure of the heat pipe: capillary, entrainment, and boiling limits. The final limitation is the recently developed frozen startup limit (32); violation of this limit prevents successful startup from the frozen state. The author calculated these limits for each of the three heat pipes. Four of the classical limits are displayed graphically in Figure 8. The vertical axes are scaled differently to adequately depict the performance envelopes.

Classical Performance Limitations. The six classical performance limits were calculated for operation temperatures up to 500 °C. The calculations were based upon the theory and assumptions presented by Faghri (6:221-264). The results were

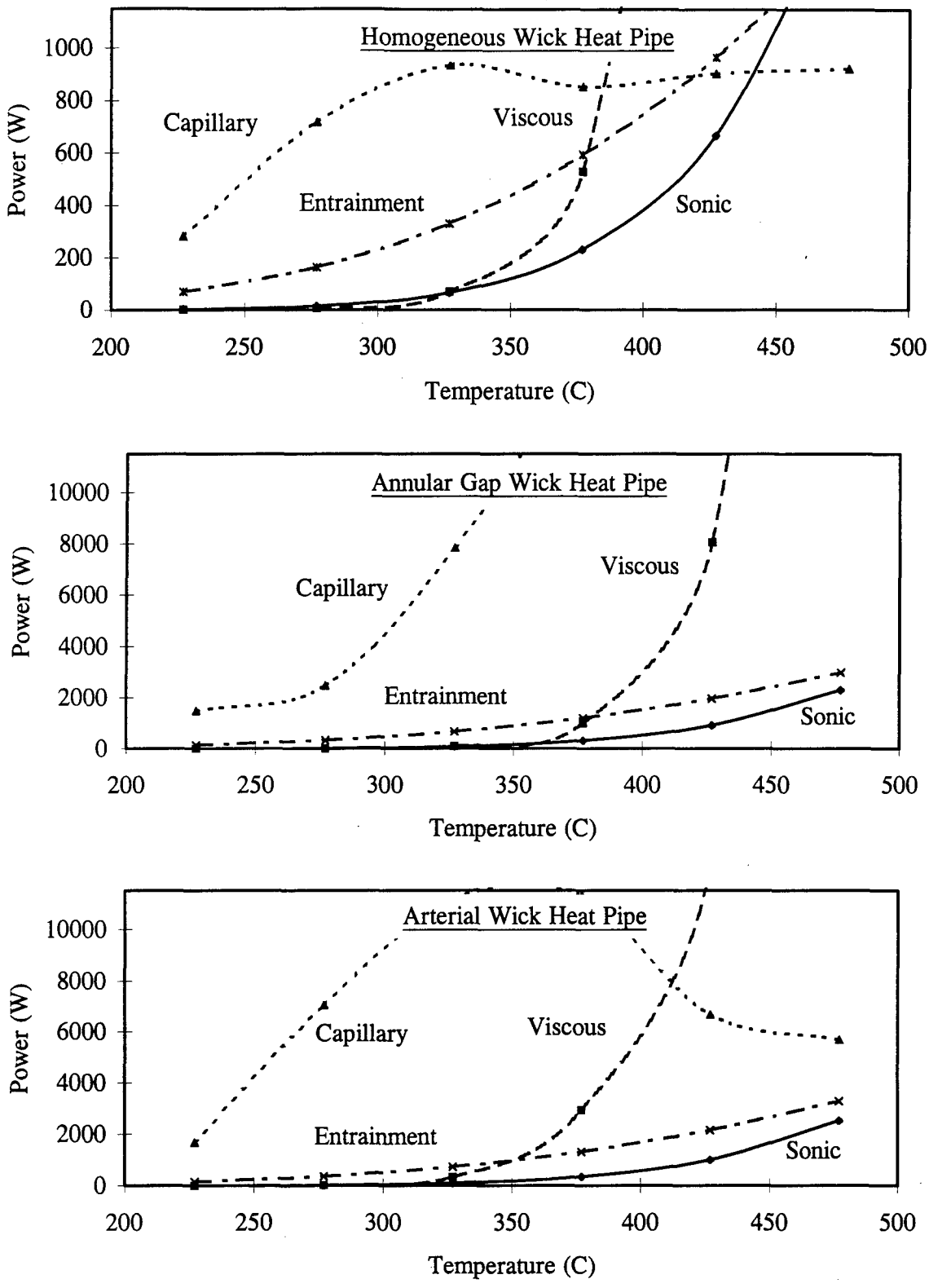

Figure 8 : Heat Pipe Performance Envelopes

validated against Los Alamos National Laboratory analyses conducted with the steady-state heat pipe code HTPIPE (33). In some cases, the work of other authors served as further validation.

The vapor flow is in a rarefied condition at very low temperatures of operation. Under this condition, minimal vapor propagates along the heat pipe and heat transfer is limited. The vapor continuum limitation states that significant heat transfer will not occur until continuum flow is established. The vapor temperature associated with transition to continuum flow is a function of vapor properties and heat pipe dimensions (6:262):

$$T = \frac{\sqrt{2}\pi d^2 p_v Kn D_v}{1.051\kappa} \tag{1}$$

where d is effective molecular diameter, p_v is vapor pressure, Kn is Knudsen's number, D_v is vapor passage diameter, and κ is Boltzmann's constant. The effective molecular diameter for potassium is 4.44 angstroms (34). Continuum vapor flow exists when $Kn \leq 0.01$. This equation was solved iteratively for each heat pipe since the saturation vapor pressure is a function of vapor temperature. The vapor transition temperatures are 313 °C, 305 °C, and 303 °C for the homogeneous, annular gap, and arterial wick heat pipes respectively. These values compare favorably with Tournier's calculation of 297 °C for a potassium heat pipe of similar dimensions (34). The vapor continuum limitation is encountered during startup from the frozen state until the vapor in the evaporator reaches the continuum flow transition temperature (6:262-263).

At very low temperatures, the vapor pressure difference between the evaporator and condenser is extremely small. In such cases, the viscous forces may be larger than the vapor pressure gradients and thus prevent vapor flow. This condition is the viscous limitation. It is a function of heat pipe dimensions and vapor conditions in the evaporator (6:257):

$$Q_{viscous} = \frac{A_v D_v^2 h_{fg} \rho_o p_o}{64 \mu L_{eff}} \tag{2}$$

where A_v is vapor passage cross-sectional area, h_{fg} is heat of evaporation, ρ_0 and p_0 are stagnation vapor density and pressure in the evaporator, μ is dynamic viscosity, and L_{eff} is effective heat pipe length. The calculations were verified by the work of Ivanovskii et al (35:75-77). This limitation is also temporary; heat transfer is constrained by other phenomenon as the vapor temperature increases (6:255-257).

After establishment of continuum flow, the pressure in the evaporator accelerates the vapor until it reaches a maximum velocity at the evaporator exit. The low downstream vapor pressure of a liquid metal heat pipe during startup can lead to a sonic vapor velocity at the evaporator exit. The limitation of such flow is similar to a converging-diverging nozzle with constant mass flow rate, where the evaporator exit corresponds to the nozzle throat. This choked flow condition is termed the sonic limitation. A closed-form relation for the sonic limit heat transfer rate can be obtained if a uniform evaporation rate is assumed (6:249):

$$Q_{sonic} = A_v h_{fg} \rho_o \left[\frac{K' R_g T_o}{2(K'+1)} \right]^{1/2} \tag{3}$$

where K' is ratio of specific heats, R_g is the gas constant, and T_0 is stagnation vapor temperature in the evaporator. This limitation is similar to the viscous limitation in that it is typically encountered during the startup transient but does not represent failure of the heat pipe. As shown in Figure 8, the heat transfer constraint of these heat pipes is predicted to transition from the viscous limit to the sonic limit during startup. These values agree with the results of Brennan and Kroliczek (36:172-173). Further increases in heat pipe temperature raise the vapor pressure in the condenser. The pressure eventually becomes sufficient to maintain a subsonic vapor velocity at the evaporator exit. This condition results in operation below the sonic limit (6:248-249).

The capillary forces established by the wick structure circulate the working fluid. Circulation ability is limited by the maximum sustainable capillary pressure. When the sum of the liquid and vapor pressure drops exceeds the maximum sustainable capillary pressure, evaporator dryout occurs and leads to operational failure of the heat pipe. The following equation provides the maximum heat transfer rate sustainable for a given wick structure (6:227):

$$Q_{capillary} = \frac{4\sigma / r_{eff}}{L_{eff}(F_l + F_v)} \tag{4}$$

where σ is surface tension, r_{eff} is effective pore radius of the wick, and F_l and F_v are liquid and vapor friction coefficients. This equation neglects the pressure drops associated with evaporation and condensation. The gravity term is also eliminated since the heat pipes were operated under microgravity conditions. Operational failure will occur if the capillary limitation is reached (6:224-228).

The opposite flow of liquid and vapor creates a shear force at the liquid-vapor interface. At high vapor velocities, liquid entrainment into the vapor flow may result. Excessive entrainment starves the evaporator of fluid and leads to dryout and failure of the heat pipe. This heat transfer rate is identified as the entrainment limit (6:255):

$$Q_{entrainment} = A_v h_{fg} \left(\frac{\sigma \rho_v}{2 r_{hyd}} \right)^{1/2} \quad (5)$$

where ρ_v is vapor density and r_{hyd} is hydraulic radius of a wick surface pore.

Entrainment in capillary-driven heat pipes has not been observed experimentally. The capillary structure of the wick most likely inhibits liquid separation at the liquid-vapor interface. The nature of this interaction is not fully understood. It is anticipated that the entrainment limit exceeds the capillary limit for capillary-driven heat pipes (6:255). The entrainment calculations for the three heat pipes compare favorably with the work of Brennan and Kroliczek (7:41-42) but neither set of calculations consider the inhibiting effect of the capillary structure.

The boiling limit occurs when excessive heat flux to the evaporator causes the working fluid to boil in the wick. A critical bubble radius exists for given working fluid properties and liquid superheat. A bubble will disappear if the radius is less than the critical radius but will grow if it is greater. A stable or growing bubble between the heat pipe wall and working fluid results in development of a hot spot. If boiling is severe, it will lead to evaporator dryout and failure of the heat pipe. As the evaporator temperature increases, the heat input required for boiling decreases (6:246):

$$Q_{boil} = \frac{2\pi L_{evap} k_{eff} \Delta T_{crit}}{\ln(r_i / r_v)} \tag{6}$$

where L_{evap} is evaporator length, k_{eff} is effective wick thermal conductivity, ΔT_{crit} is superheat required for boiling, r_i is pipe inner radius, and r_v is vapor passage radius. The superheat required for liquid metals is much greater than for lower temperature working fluids such as water. For this reason, the boiling limit is seldom encountered in liquid metal heat pipes. This limit exceeds the other limits by several orders of magnitude for the three heat pipes in this study and therefore is not shown in Figure 8 (6:232-248).

Frozen Startup Limitation. The frozen startup limitation for liquid metal heat pipes was recently developed and introduced by Cao and Faghri (32). Improperly designed liquid metal heat pipes may encounter this limitation during startup from the frozen state. If the condensation rate of vapor onto frozen working fluid exceeds the melt rate of working fluid, the evaporator will become depleted. The ratio of the latter to the former must exceed unity for successful startup (6:337):

$$\frac{\phi \rho_l A_w h_{fg}}{C(T_{mel} - T_\infty)} \geq 1 \tag{7}$$

where ϕ is wick porosity, ρ_l is liquid density, A_w is cross-sectional area of working fluid in the wick, C is heat capacity per unit length of wall and wick, T_{mel} is working fluid melt temperature, and T_∞ is temperature of the surroundings. For a given working fluid, an increase in fluid inventory will increase this ratio and improve the safety margin for heat pipe startup. The homogeneous, annular gap, and arterial wick heat pipes have

frozen startup limit values of 6.7, 12.3, and 4.3 respectively. The annular gap wick value is notably greater than the other two due to the significant potassium overcharge discussed in the previous chapter. These heat pipes should not experience difficulties during startup from the frozen state (6:263-264,333-338).

Thermal Vacuum Test

Thermal vacuum tests (37) were conducted by Phillips Laboratory in a 17 cubic meter thermal vacuum chamber at Sandia National Laboratory. The objective of the tests was operational verification of the heat pipes and experimental control unit in the expected flight environments. The platform was tested in the fully integrated flight configuration with the heat pipes in a horizontal position to minimize gravity effects. The tests were conducted at vacuum pressures between 10^{-8} and 10^{-6} torr to prevent convective heat transfer between components. The experimental platform thermocouples recorded temperatures of the heat pipes, electronics, and canister interior; twenty additional thermocouples monitored temperatures of the power supply and canister exterior.

Each heat pipe cycled twice through a startup and shutdown scenario. The startup scenario was initiated by a 30 minute thaw period to melt the frozen potassium in the evaporator; the evaporator heater operated for 15 minutes at heater power levels of 80 W and 135 W. A 15 minute ramp to the maximum power of 280 W followed the thaw period. A heater power of 280 W was maintained for 45 minutes until steady-state operation was achieved. Power was then removed from the heater and the heat pipe

cooled for 4 hours. The first cycle occurred at a chamber temperature of 10 °C and the second occurred at -5 °C.

All experimental control unit components performed as designed. Heat pipe operation appeared consistent with theory but a software error prevented complete storage of the temperature profiles during transient and steady-state operation. The error was not discovered in time to allow a repeat of the tests. This prohibited a complete pre-flight characterization of the startup transients. However, at least three temperature profiles at various times during the startup transient were obtained for each heat pipe. This data is compared against flight data in Chapter Five.

Summary

Microgravity performance envelopes were calculated for each of the heat pipes. These envelopes indicated heat pipe operating regions and anticipated limitations during startup and steady-state operation. Thermal vacuum tests verified satisfactory performance of the heat pipes and experimental control unit. Thermal vacuum data was obtained for comparison against flight data, although a partial data loss prevented complete startup characterization.

IV. Flight Experiment

Introduction

The experiment was flown on mission STS-77 aboard the Space Shuttle Endeavour during 19-28 May 1996. This chapter describes the test scenarios developed for the mission, procedures for test execution, and the test environment.

Test Scenarios

The three experimental objectives led to the development of four test scenarios; the objectives were characterization of startup behavior, comparison of microgravity and ground performance, and assessment of three heat pipe designs. A series of three tests applied to the first objective. One test repeated the thermal vacuum test scenario executed on the ground prior to the flight experiment. This test also addressed the second objective. Steady-state performance tests at seven heat loads provided data for comparison of the three heat pipe designs. These tests complied with the third objective. All tests began from the frozen state.

Startup Characterization Tests. Three startup characterization tests addressed the first two experimental objectives. The first test, titled Startup, was a repeat of the thermal vacuum tests. The other two tests resulted from the work of Jang and his associates (38). The numerical results of their mathematical model highlight two important findings: a small amount of heat input at the condenser aids startup from the frozen state and a starved evaporator prevents a successful startup. The second and third tests, titled Preheated Condenser and Starved Evaporator, investigated these two issues.

The Startup Test incorporated the same heat input profile as the thermal vacuum tests. This profile will be shown later with the experimental data in Chapter Five. The results established the baseline for startup characterization of the heat pipes and provided a comparison between ground and flight test data. This test was conducted twice on each heat pipe to assess performance repeatability.

The Preheated Condenser Test investigated the effect of heat input at the condenser prior to startup. A power of 65 W applied to the condenser heater for 90 minutes fully melted the potassium in that section. Power was then removed from the condenser heater and the heat pipe entered the Startup Test profile.

The Starved Evaporator Test examined startup effects of an unfavorable distribution of frozen working fluid. A secondary objective was evaluation of recovery strategies if startup failed under adverse conditions. Liquid redistribution was attempted through vapor migration from the evaporator and subsequent condensation onto the frozen fluid in the condenser. The evaporator heater operated at 60 W to melt the potassium in the evaporator but was shutdown after 30 minutes to prevent the melt of frozen potassium in the condenser. This scenario generated vapor in the evaporator and ensured solidification of condensed vapor in the condenser (39). The heat pipe cooled to a fully frozen state prior to execution of the Startup Test scenario.

Steady-state Tests. The third objective was addressed through a series of steady-state tests at seven heater power levels: 80, 105, 135, 165, 200, 240, and 280 watts. Continuum front advancement was observed and compared for each of the heat pipes at

the various levels. Operation at these low power levels revealed the minimum power required for each heat pipe to achieve an isothermal, or fully operational, condition.

Test Execution

Communication Sequence. Ground support equipment, pictured in Figure 9, controlled the experiment and stored data during the mission. The Payload Operations Control Center at NASA Goddard Space Flight Center housed this equipment. NASA Johnson Space Center established a communication link between the Control Center and the space shuttle with assistance from a Tracking and Data Relay Satellite (TDRS). The Hitchhiker avionics aboard the shuttle received the commands and routed them to the experimental control unit in the flight canister. Figure 10 illustrates this sequence.

Figure 9 : Ground Support Equipment in Payload Operations Control Center

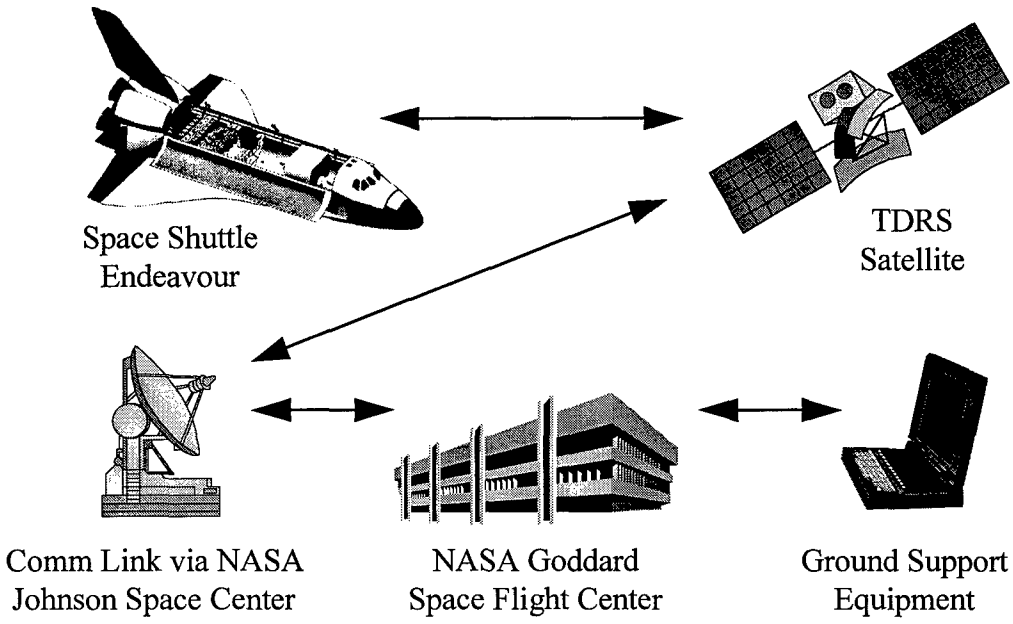

Figure 10 : Communication Link

Test Sequence. The flight computer was programmed to regulate heater power for specific time intervals prior to initiation of a test sequence. Test execution began with a command from the ground support equipment and continued autonomously under control of the flight computer. One heat pipe operated at a time. Each heat pipe cooled below the solidification temperature of potassium, 64 °C, before initiation of the next heat pipe test. This step allowed heat dissipation from the canister and ensured consistent environment temperatures for the tests.

Data Acquisition. The communication link described above also provided a telemetry path to the ground. Telemetry data was simultaneously stored by NASA and post-processed by the ground support equipment. National Instruments' LabView software processed the data and facilitated real-time analysis.

Test Environment

The platform operated continuously from 9 hours after launch to 24 hours prior to reentry; this yielded a total test time of 200 hours. Operations continued during shuttle stationkeeping and satellite rendezvous maneuvers. Throughout these maneuvers, the shuttle did not sustain a bay-to-sun configuration. Consequently, favorable temperature and pressure conditions were maintained within the canister. A thermistor positioned in the canister below the experimental platform recorded temperatures between 10 °C and 35 °C, consistent with payload bay temperatures. Canister pressures were maintained between $5 \cdot 10^{-6}$ and $5 \cdot 10^{-5}$ torr, below the 10^{-4} torr required for negligible convective heat transfer (2).

A signal loss between the shuttle and ground occurred at 90 minute intervals for 5 to 15 minute durations when the shuttle lost view of a TDRS satellite. This resulted in a data loss since the platform did not possess data storage capability. Tests were scheduled to avoid this period during critical moments, such as power level changes during startup transients. Entire startup transients occurred between signal losses when possible.

Summary

The test scenarios executed during the mission addressed all the experimental objectives. The scenarios were programmed with the ground support equipment and conducted autonomously by the flight computer. A telemetry link with the shuttle permitted real-time analysis and storage of the experimental data. Consistent environmental conditions for each test ensured the accuracy of the test results.

V. Post-flight Analysis

Introduction

Experimental results and analyses are grouped by experimental objective. The three objectives were characterization of startup behavior, comparison of microgravity and ground performance, and assessment of three heat pipe designs. Experimental data consisted of heater and heat pipe wall temperatures as a function of time for the various test scenarios. It is shown later in this chapter that wall temperatures closely approximate vapor temperatures. Heat pipe theory specifies an isothermal region between the evaporator exit and continuum front. However, several thermocouples exhibited a deviation from this condition. The thermocouples repeated these deviations identically during ground and flight tests. These deviations are therefore attributed to thermocouple attachment inconsistencies rather than thermocouple accuracy; the deviations do not reflect true temperatures.

Objective 1 : Startup Characterization

Startup Test. Heater power and heat pipe wall temperature profiles for this test are illustrated in Figures 11 and 12 respectively. The startup behavior of the homogeneous wick heat pipe was consistent with theory (11:114-119). The continuum front, marked by the sharp temperature gradient in Figure 12, did not advance until vapor in the evaporator exceeded the continuum flow transition temperature of 313 °C. The calculation of this temperature is discussed in Chapter Three. Heat transfer between

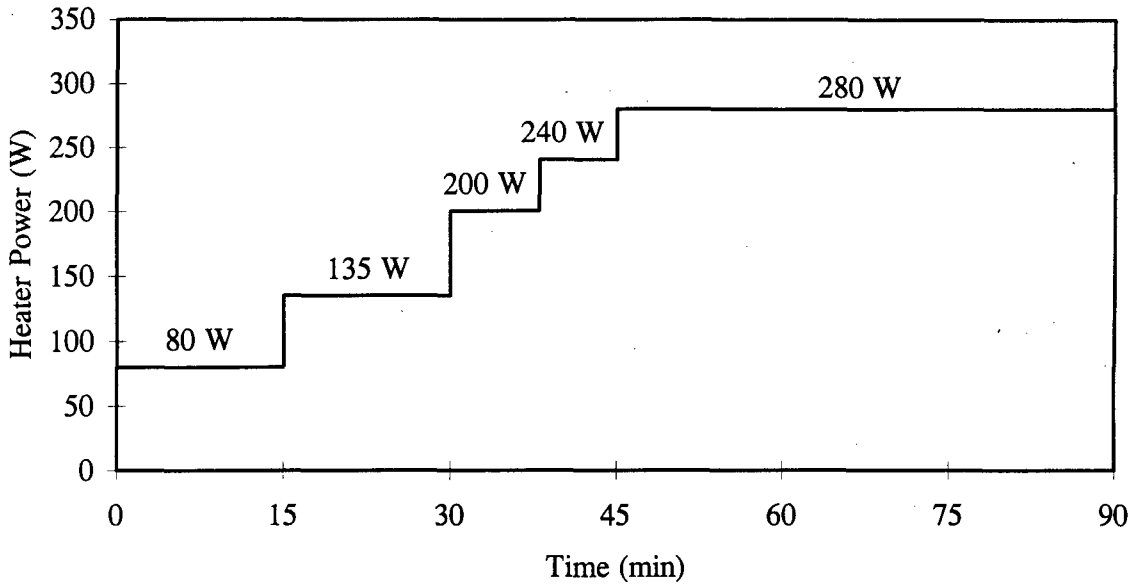

Figure 11 : Startup Test Power Profile

the evaporator and condenser was limited prior to advancement of the front due to the rarefied flow condition beyond the front. Heat transfer increased as the continuum front propagated along the condenser. After 30 minutes, the front had advanced 18 cm past the evaporator exit. The continuum front continued its progression towards the end of the condenser during the startup transient. The heat pipe was nearly isothermal between the evaporator exit and continuum front throughout the test; the temperature drop was typically 10 °C to 15 °C.

The annular gap wick heat pipe was equally responsive to startup from the frozen state. The continuum front advanced after vapor exceeded the transition temperature of 305 °C in the evaporator. This advancement is shown in Figure 12. Advancement of the front initially occurred more rapidly than in the other two heat pipes. After 30

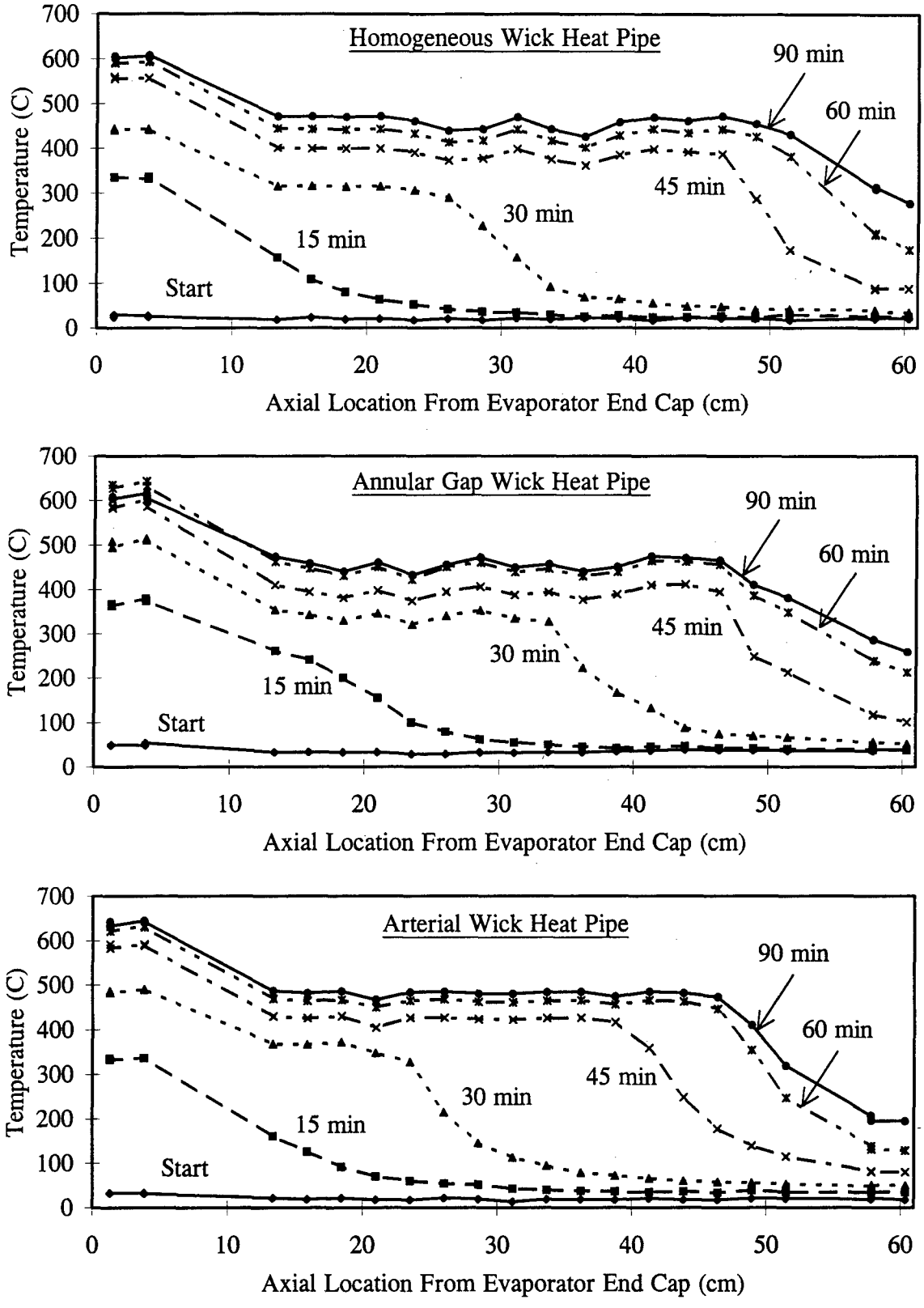

Figure 12 : Startup Test Temperature Profiles

minutes, the front was located 24 cm past the evaporator exit compared to 18 cm and 14 cm for the homogeneous and arterial wick heat pipes respectively. After the potassium was completely melted, vapor swept the excess fluid to the end of the condenser; this behavior was anticipated (11:9). The pool of excess fluid limited the effective length of the condenser to 37 cm. This pool of excess liquid is evidenced by the temperature drop at the end of the condenser. The temperature drop is due to the long conduction path of the liquid. The stationary location of the temperature gradient near the end of the startup transient indicates the boundary of the excess fluid. A liquid pool length of 14 cm corresponds to excess liquid mass calculations as well as ground test observations (1). Again, the heat pipe was nearly isothermal along the effective length of the condenser throughout the test.

The startup behavior of the arterial wick heat pipe, as shown in Figure 12, was also consistent with theory. Advancement of the continuum front began after the vapor reached the transition temperature of 303 °C. The front progressed steadily along the condenser and extended 37 cm past the evaporator exit at the end of the startup transient.

These tests were conducted twice to examine repeatability. The temperature profiles shown in Figure 12 were duplicated for each heat pipe in the subsequent tests.

Preheated Condenser Test. Temperature profiles for this test are compared with those of the Startup Test in Figure 13. In all the heat pipes, the potassium was completely melted in the condenser prior to initiation of the startup profile; heat pipe wall temperatures were 350 °C near the condenser heater and 80 °C to 100 °C near the evaporator.

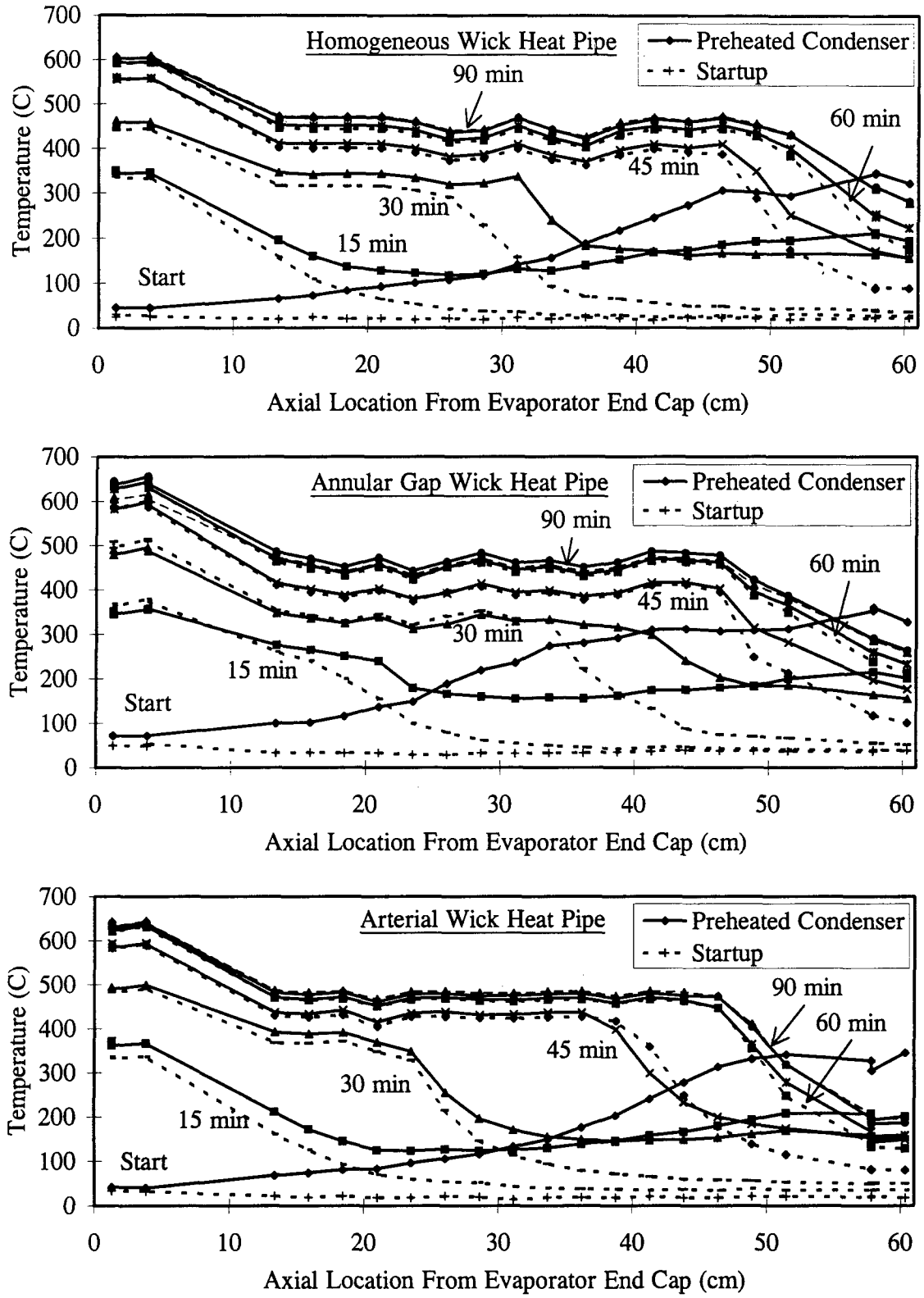

Figure 13 : Startup Test Versus Preheated Condenser Test Temperature Profiles

In this test, the heat pipe condenser was warmer throughout the startup transient. Advancement of the continuum front initially exceeded that of the Startup Test scenario. The temperature profiles of the two scenarios coincide after 45 minutes for the homogeneous and annular gap wick designs and after 30 minutes for the arterial wick design. A preheated condenser accelerated startup initially but did not affect the steady-state condition or the time required to achieve it.

Starved Evaporator Test. The scenario outlined in the previous chapter did not allow enough time for sufficient migration of vapor into the condenser to achieve an adverse distribution of frozen working fluid (8). Heat input to the evaporator was applied at the lowest heater power of 60 W but discontinued after 30 minutes due to melt of potassium within the condenser. Continuum flow had only begun to develop, therefore little working fluid migrated due to the low vapor pressure of potassium in the rarefied state (34). As a result, the change in working fluid distribution was insufficient to alter startup temperature profiles. The distribution could have been altered if stronger thermal coupling had existed between the condenser and surroundings; such coupling could have maintained the condenser at a temperature below the melt temperature of the working fluid.

Shutdown Temperature Profile. Shutdown of the heat pipes was monitored to determine the distribution of potassium at ambient temperature. Typical profiles are shown in Figure 14. Each heat pipe cooled from a temperature of approximately 500 °C to 100 °C in 2 hours. The heat pipes were nearly isothermal as the potassium in the condenser reached the solidification temperature of 64 °C. The temperature difference

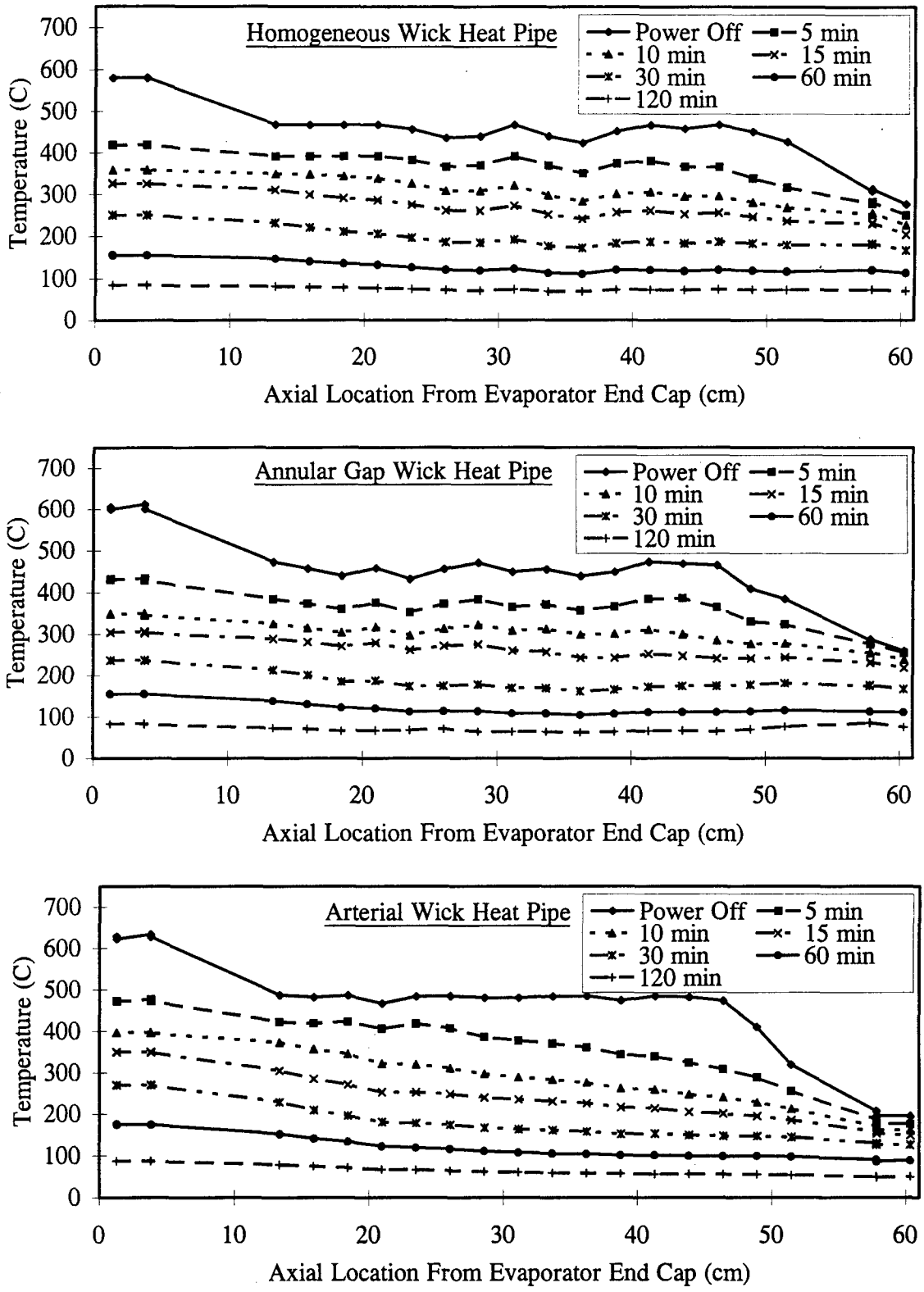

Figure 14 : Shutdown Temperature Profiles

between the evaporator and condenser ranged from 4 °C to 28 °C for the three heat pipes. The time delay between solidification of potassium in the condenser and evaporator ranged from 12 to 40 minutes, with solidification occurring first in the condenser region. These time delays and low temperatures result in a maximum migration of 3 micro-grams of potassium from the evaporator after solidification began in the condenser. This behavior occurred in all tests and indicated the working fluid was uniformly distributed in the frozen state. An uneven potassium distribution or blockage of frozen working fluid could have prevented restart through evaporator starvation (24).

Restart. Each heat pipe experienced a minimum of nine thermal cycles, with all cycles initiated from the frozen state. The startup behavior was consistent in each scenario. The Startup Test was conducted twice and identical behavior was demonstrated in both tests. These observations testify to the robustness of the heat pipes as well as the repeatability in their performance.

Frozen Startup Limitation. As defined in Chapter Three, the ratio of melt rate to vapor freeze rate must exceed unity for successful startup. The values for the homogeneous, annular gap, and arterial wick designs are 6.7, 12.3, and 4.3 respectively. These values indicate robustness regarding startup behavior of the heat pipes. Experiment results support this prediction. The heat pipes did not experience difficulties during startup from the frozen state in any of the tests. This startup behavior is consistent with that of other liquid metal heat pipes during ground experiments (22; 40). The large thermal conductivity of liquid metals allows the fluid to melt by conduction before significant evaporation of the liquid occurs.

Objective 2 : Flight and Ground Performance Comparison

Flight Versus Ground Startup. A partial loss of ground thermal vacuum test data prevented complete startup characterization prior to the flight test. However, data was obtained at several points during the ground startup of each heat pipe. This thermal vacuum data is compared with the flight data in Figure 15. Data from both tests were available at 5, 20, and 65 minutes for the homogeneous wick heat pipe and 10, 25, and 55 minutes for the annular gap and arterial wick designs.

The flight performance of the homogeneous and arterial wick heat pipes compared favorably with ground thermal vacuum performance; recall the heat pipes were positioned horizontally during ground tests to minimize the effects of gravity. Only the startup temperature profiles for the annular gap wick design were significantly different. The ground thermal vacuum test data is inconsistent with heat pipe theory, thermal proof test data, and flight test data. The temperature profile at 25 minutes does not exhibit a sharp gradient and thus indicates the absence of a continuum front. Also, the profile at 55 minutes does not indicate the presence of excess working fluid pooled in the condenser. This pool was observed during all subsequent flight tests as well as the preceding thermal proof tests at Los Alamos National Laboratory (1) and Phillips Laboratory (31). The lack of further ground test data prevents a complete assessment of the discrepancies; however, the differences are likely due to altered test conditions, such as an uneven distribution of working fluid (41). Further investigation is required to resolve these discrepancies.

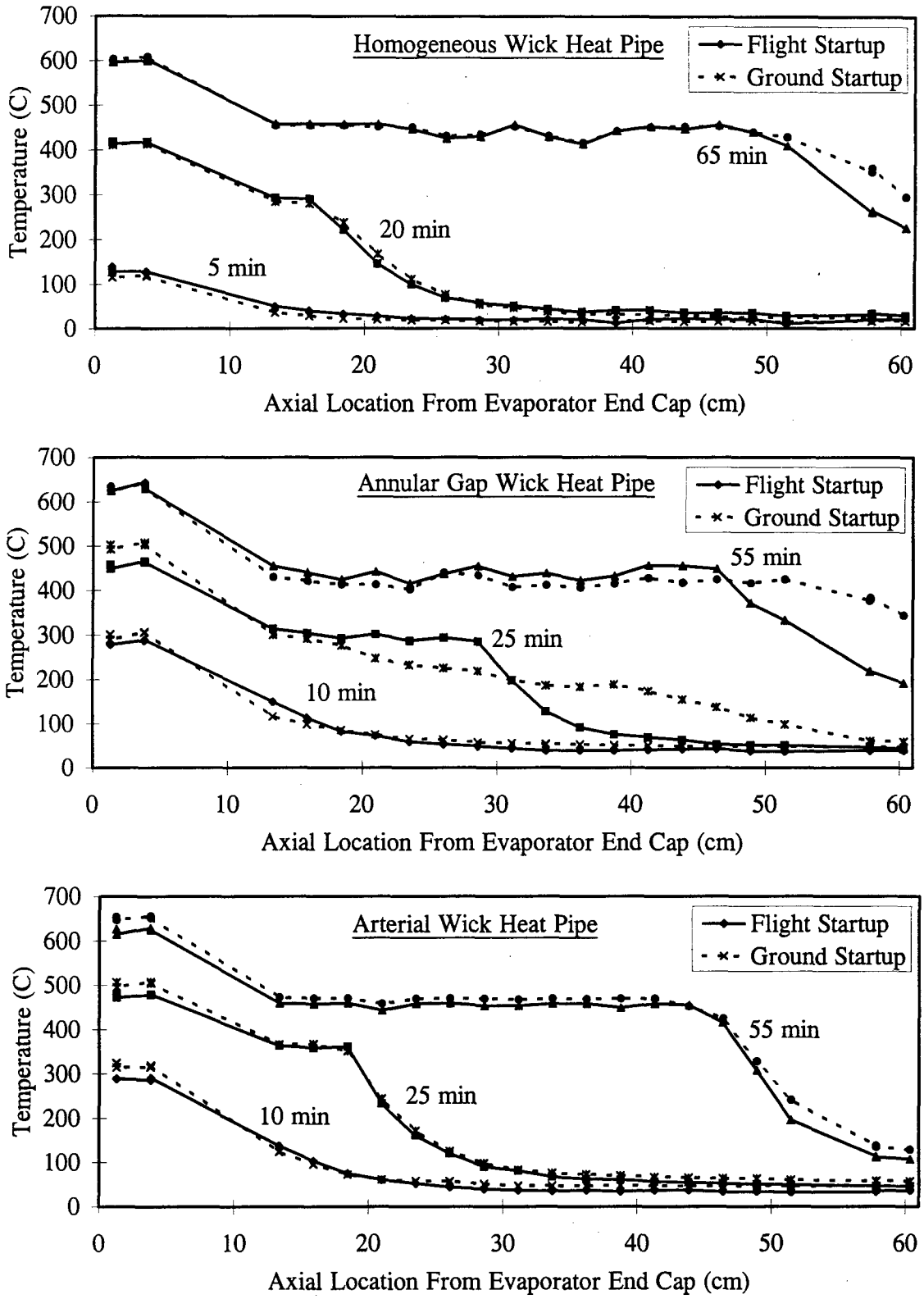

Figure 15 : Flight Versus Ground Startup Test Temperature Profiles

Flight Versus Ground Shutdown. The first flight test scenario was a steady-state test initiated with a 105 W step input. This test was repeated in the final series of flight tests. The first execution was preceded by a shutdown under the influence of gravity at the end of the ground thermal vacuum test. This shutdown probably resulted in pooling of the liquid along the bottom of the heat pipe and an uneven circumferential distribution of frozen potassium. The final execution was preceded by a shutdown without the influence of gravity and most likely resulted in an even distribution of the fluid about the circumference. However, if the different distributions did occur, they did not affect subsequent startup behavior. The startup temperature profiles were identical for both tests of all three heat pipe designs.

Objective 3 : Design Assessment

Calculations of heat pipe energy throughput and evaporator and condenser temperatures led to the calculation of thermal resistance values for the heat pipes. General steady-state behavior and operation with respect to the predicted performance envelopes were also investigated.

Evaporator Heater Efficiencies. Evaporator heater efficiencies were calculated for the seven steady-state power levels to determine heat pipe energy throughput. The heat loss from the heater was determined by a radiation analysis. The energy transmitted through each pipe was calculated by subtraction of this heat loss from the heater power.

Heat loss from the heater was calculated by the author through a two-surface enclosure radiation analysis (42:806-815); conduction through the evaporator end cap

was neglected since the heat pipe was insulated from the top end plate. In reality, the enclosure had six different surfaces as shown in Figure 16: top end plate, enclosure with molybdenum shield, unshielded enclosure end, gap between enclosure end and heat pipe, heater, and small sections of the heat pipe beyond each end of the heater. Temperature data was available for only the heater and shielded surface of the enclosure. This limited the radiation analysis to a two-surface approximation. The heat pipe and heater were treated as the first surface and the other entities composed the second surface. The primary heat transfer path was between the heater and shielded portion of the enclosure. The view factor from the heater to the shield is 0.94 for the six-surface case and decreases only 3% for the two-surface case. The results of the two-surface analysis are the best that can be expected given the limited available data.

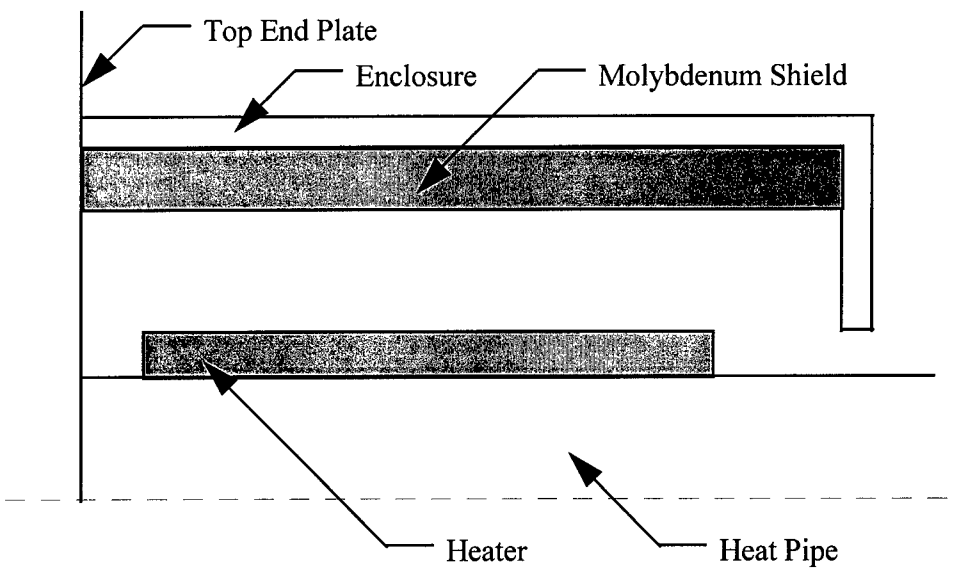

Figure 16 : Evaporator Heater Enclosure

For the radiation analysis, the surfaces were treated as isothermal, opaque, diffuse, and gray. The temperature of the heater was measured with thermocouples. The temperature of the molybdenum shield inner surface was determined through calculation of the thermal resistance between the heater and the measured enclosure temperature (42:98). This resistance was a function of shield layer separation and surface emissivities. A separation of 0.10 cm was assumed for the shield layers. Due to oxidation, the following emissivity values were used for the surfaces: 0.67 for the stainless steel heater jacket, 0.65 for the molybdenum shield inner layer with an incremental decrease to 0.50 for the outer layer, and 0.40 for the stainless steel enclosure interior (42:A27). The total thermal resistance between the heater and enclosure was 900 °C/W; the shield contribution was 710 °C/W. These resistances produce a temperature difference of 206 °C across the shield for a heater temperature of 600 °C. This difference agrees with the 200 °C temperature difference experienced in ground thermal vacuum tests (43). The surface temperatures of the shield inner layers were calculated for the seven steady-state power levels.

Heater efficiencies were determined from heat loss calculations. The surface areas, emissivities, and temperatures of the shield and heater were used in the radiation analysis to calculate heat loss. Heater efficiency is defined as the ratio of power transmitted into the heat pipe to the power output of the heater:

$$\eta = \frac{Q_{transmitted}}{Q_{heater}} \tag{8}$$

Heater efficiencies ranged from 72% to 84% for the three heat pipes and seven power

levels with a maximum standard deviation of 4.2%. Heater efficiencies, depicted graphically in Figure 17, increased slightly as heat load increased. This resulted from decreased heat pipe resistances as discussed below.

Heat Pipe Wall Temperature Corrections. The thermocouples, except those mounted on the evaporator and condenser heater jackets, recorded wall temperatures along the heat pipe. Calculation of evaporator wall temperatures beneath the heaters was required for steady-state analyses. Analyses did not require calculation of the wall temperatures beneath the condenser heaters.

Evaporator wall temperatures were determined from heater jacket temperatures, heater power, heater efficiency, and contact resistances. The heater element was treated as a radial conduction problem with thermal energy generation (42:108-119). Radial temperature variation through the heater was found by solution of the general two-

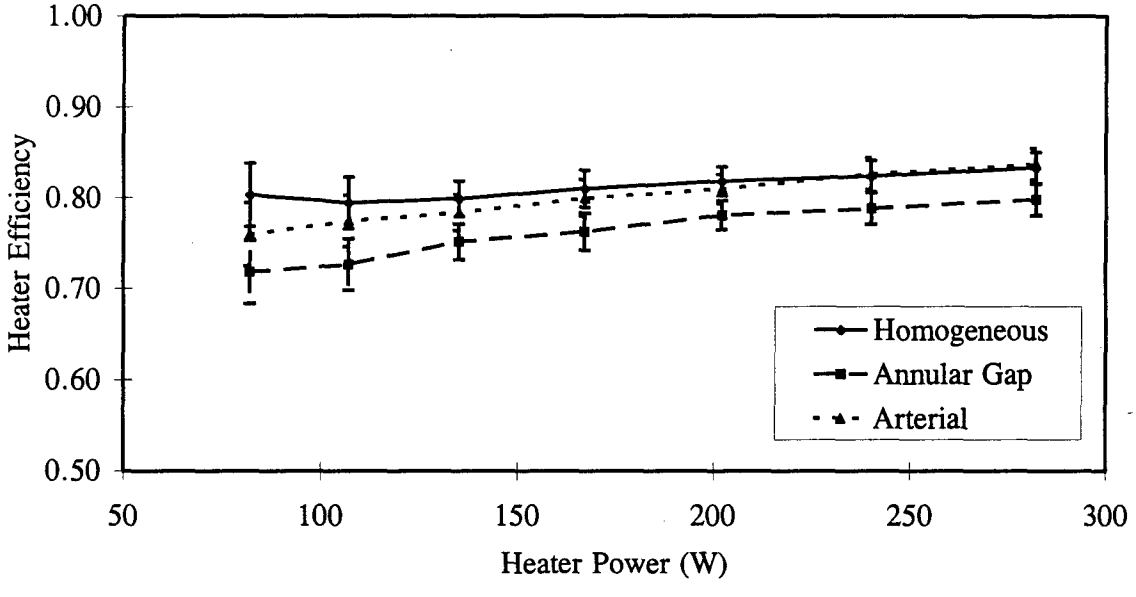

Figure 17 : Heater Efficiencies

dimensional heat conduction equation. Two boundary conditions were required to solve this problem. The jacket temperature provided the first boundary condition. The second boundary condition was the radial location of the zero temperature gradient within the heater element. Uniform heat generation was assumed. The location of the zero gradient was approximated as the radial location that corresponded to the percent of energy that entered the heat pipe. Nominal contact resistance values between the heater and heat pipe wall and between the heater and heater jacket were obtained from Incropera and DeWitt (42:87). These values were $20 \cdot 10^{-4}$ $m^2 \cdot °C/W$. The boundary conditions and contact resistances allowed for calculation of the evaporator wall temperatures; calculations were made for the seven steady-state power levels. These temperatures were typically 20 °C to 60 °C lower than the measured heater jacket temperatures for the range of heater powers. The evaporator wall temperatures were required for the thermal resistance calculations described below.

All performance calculations were based on the effective condenser length; this length was defined by the location of the sharp temperature gradient at the continuum front. Condenser temperatures were treated as the average wall temperature along the effective length. The effective condenser did not include the region beneath the condenser heater in any of the test scenarios. Therefore, calculation of wall temperatures beneath the condenser heaters was not required.

Heat Pipe Thermal Resistances. Thermal resistance of an object is defined as the ratio of temperature drop to energy transmitted. Theoretical and experimental thermal resistances were calculated for the heat pipes. These calculations are described below.

The heat transfer resistance path in the heat pipes is approximated as a series path between the evaporator and condenser. Radial resistances are due to conduction through the wall and wick and evaporation and condensation at the liquid-vapor interface; these resistances are in series. Axial resistances between the evaporator and condenser are due to vapor transportation and conduction along the wall and wick; these resistances are in parallel. The thermal resistance of vapor flow is two to three orders of magnitude less than the thermal resistance of conduction along the wall and wick. Therefore, the latter path is neglected and the remaining resistances are modeled as a series path.

The theoretical resistances for each segment were calculated from Chi's (11:73) relations and verified with the approach of Dunn and Reay (5:80-81). The thermal resistances associated with evaporation and condensation were two orders of magnitude less than the other resistances and therefore neglected. Theoretical resistance calculations for the homogeneous wick heat pipe are 0.052 °C/W at 300 °C and 0.026 °C/W at 500 °C. The reduction in resistance for increased temperature occurs for two reasons. The wall and wick resistances of the condenser decrease by a factor of two due to the increased effective condenser length; the vapor resistance decreases by two orders of magnitude due to the higher vapor density associated with increased temperature. For these thermal resistances, a maximum temperature drop of 3 °C through the wall and wick is predicted at the maximum heater power of 280 W; this small temperature drop substantiates the approximation of vapor temperatures with wall temperatures.

Thermal resistance for heat pipes is defined as the ratio of the evaporator and condenser temperature difference to the heat transport rate of the heat pipe:

$$R = \frac{\Delta T}{Q} = \frac{T_{evap} - T_{cond}}{\eta Q_{heater}} \quad (9)$$

Heat pipe experimental resistances were calculated for the seven steady-state power levels and plotted as a function of heat transport rate in Figure 18.

Experimental thermal resistances during flight were between 0.83 °C/W and 1.93 °C/W for an initial transmitted power of 60 W. The experimental resistance of the annular gap wick heat pipe was initially significantly higher than other two designs due to excess working fluid pooled along the heat pipe. This excess resulted in a longer conduction path through the wick. The excess fluid was forced to the end of the condenser as it melted and the decrease of liquid in the remainder of the heat pipe decreased the resistance through the wick (11:10).

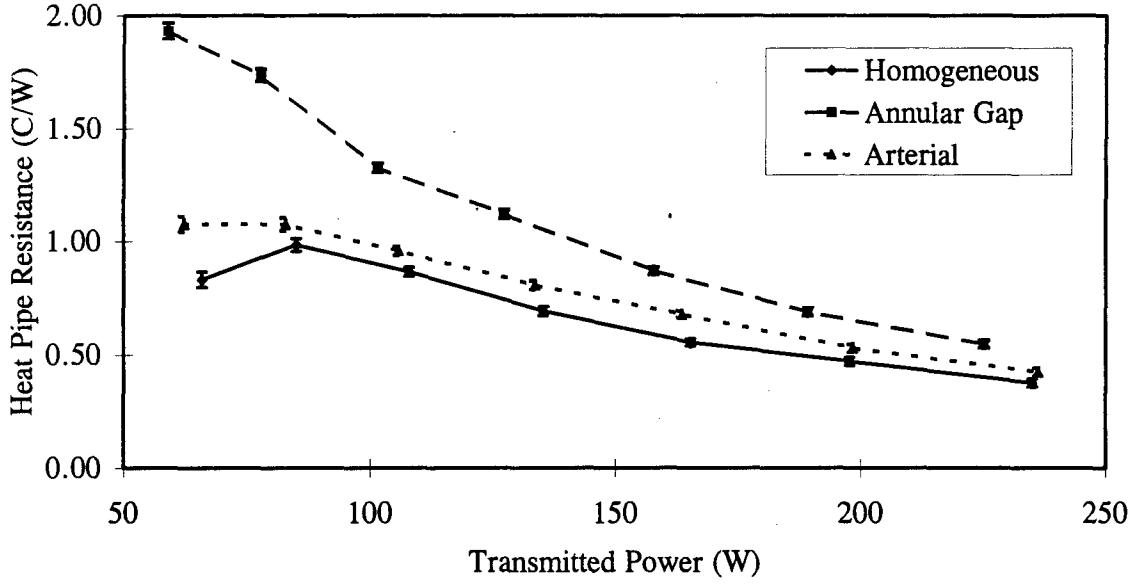

Figure 18 : Heat Pipe Thermal Resistances

The resistance of each heat pipe decreased as the heat load and effective condenser length increased and the heat pipe became fully operational. These observations are consistent with those made by Brennan and Kroliczek (7:50). The resistance values for the homogeneous, annular gap, and arterial wick heat pipes at a maximum transmitted power of 225 W to 235 W were 0.38, 0.55, and 0.42 °C/W respectively. The resistances became less dependent upon heat load as the continuum front stabilized near the end of the condenser. While the homogeneous wick design appears to have the advantage of lowest thermal resistance, the differences become insignificant from a design consideration at the higher heat transport levels.

The experimental resistance values are greater than the theoretical values by more than an order of magnitude. The wall temperature data for the homogeneous wick heat pipe at the maximum transmitted power indicates a temperature difference of 89 °C between the evaporator and condenser; the theoretical thermal resistance predicts a 6 °C temperature difference. The temperature differences during the Los Alamos National Laboratory thermal proof tests were approximately 10 °C (1); this difference agrees well with the theoretical predictions. Since gravity does not affect thermal resistance, the discrepancies between experimental and theoretical resistance values are attributed to limited available data for accurate calculations of evaporator wall temperatures.

Steady-state Tests. Performance of the homogeneous wick design was consistent with theory. As the heat input increased, the temperature increased and the continuum front progressed along the condenser. The location of the continuum front was marked

by the sharp temperature gradient. Steady-state temperature profiles for the seven heater power levels are provided in Figure 19.

The annular gap wick heat pipe functioned as the homogeneous wick heat pipe up to a heater power of 165 W. Further heat load increases raised the isothermal temperature of the annular gap wick heat pipe but the excess working fluid prevented an increase in effective condenser length. This phenomenon was also observed during thermal proof tests at Los Alamos National Laboratory (1) and Phillips Laboratory (31).

Operation of the arterial wick heat pipe was also consistent with theory. Advancement of the continuum front for increased power levels occurred in shorter increments compared to the other heat pipes. Initial condenser length was 9 cm for an 80 W heater power, compared to 22 cm and 25 cm for the homogeneous and annular gap wick heat pipes. The condenser length approached that of the homogeneous wick heat pipe at the maximum heater power of 280 W. The lengths were 37 cm and 42 cm respectively.

This behavior of the arterial wick heat pipe was also observed by Phillips Laboratory during thermal proof tests. At that time, the presence of noncondensible gas (NCG) was suspected as the cause of the behavior (31). However, several facts indicate NCG was probably not present. This behavior was not observed during thermal proof tests at Los Alamos National Laboratory (1). Therefore, if NCG were present, it must have been introduced after heat pipe manufacture. Leakage and corrosion are the most probable processes of NCG generation. All three heat pipes passed leak checks by Los Alamos National Laboratory (29) and OAO Corporation (30). In life tests at Los

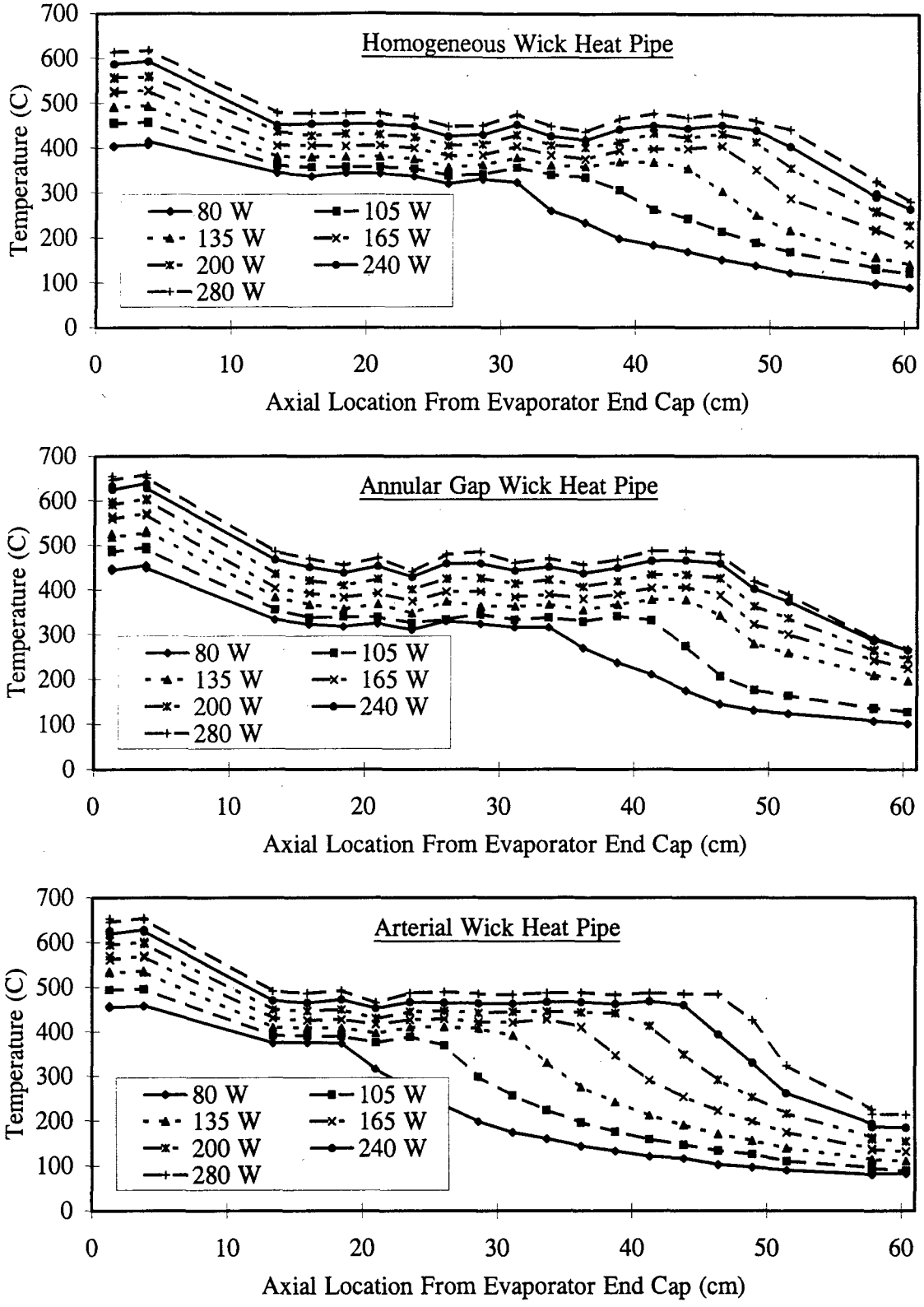

Figure 19 : Steady-State Test Temperature Profiles

Alamos, a similar Type 304 stainless steel / potassium heat pipe operated at 600 °C for 8000 hours without degradation (44). Therefore, the most probable explanation for this behavior is not NCG but rather insufficient heater power for further continuum front advancement. The Los Alamos thermal proof test was conducted at a transmitted power of 350 W while the Phillips Laboratory and flight tests were conducted at transmitted powers of 253 W and 236 W respectively. Advancement of the continuum front to the end of the condenser, as observed in the Los Alamos test, is anticipated if the heat input of the other tests had been increased to 350 W as well.

Performance Envelopes. The three heat pipes operated within their predicted performance envelopes as shown in Figure 20. As anticipated, the viscous and sonic limits restricted heat transfer at the lower temperatures, especially for the homogeneous and annular gap wick heat pipes. The arterial wick design demonstrated the largest performance margin throughout the range of power levels. This larger performance margin is more important than the small differences in heat pipe thermal resistance at the higher power levels, giving the arterial wick heat pipe a slight performance advantage over the other two designs. The heat pipes did not encounter the capillary, entrainment, or boiling limits since they operated at the lower end of their design temperature range; potassium heat pipes typically operate between 350 °C and 2000 °C (4:235). Heater limitations prevented operation at higher power levels and temperatures.

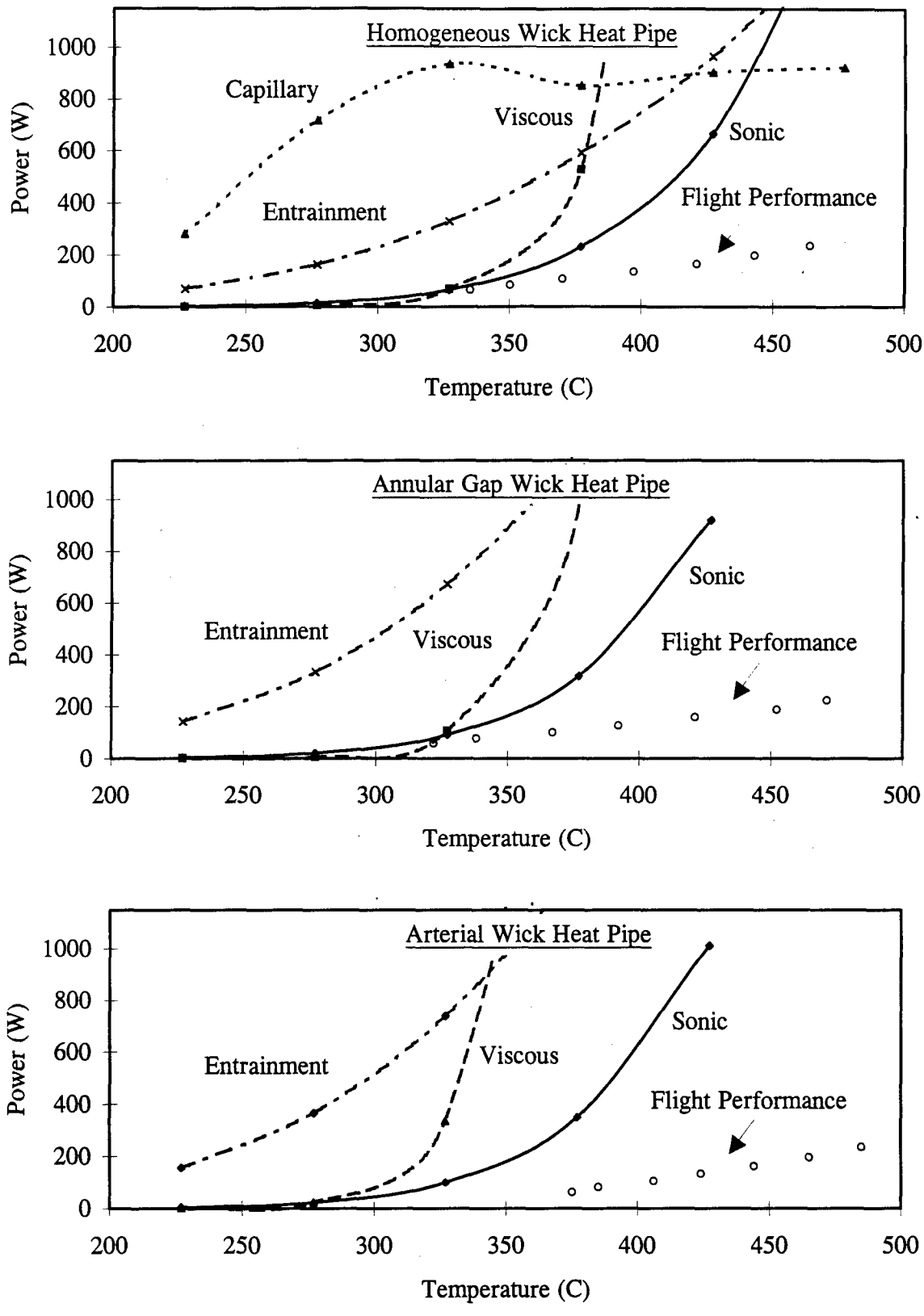

Figure 20 : Heat Pipe Performance During Flight Experiment

Summary

The startup tests successfully characterized the behavior of the heat pipes during startup from the frozen state. Numerous successful restarts demonstrated the robustness of the three designs. Microgravity performance closely matched ground thermal vacuum performance. Heat pipe operation was consistent with theory and within the predicted performance envelopes.

VI. Conclusions

Introduction

Conclusions based upon experimental results and analyses are presented according to the three experimental objectives. Recommendations for future liquid metal heat pipe investigations are also offered. These recommendations are listed in descending order of anticipated benefit-to-cost ratio.

Objective 1 : Startup Characterization

The first experimental objective was characterization of the frozen startup and restart behavior of liquid metal heat pipes in a microgravity environment. The results of the startup tests successfully characterized this behavior. Startup was consistent with theory. The continuum front, marked by a sharp temperature gradient, advanced steadily after establishment of vapor continuum flow. The heat pipe wall was isothermal between the evaporator exit and continuum front. The heat pipes cooled isothermally to provide an even distribution of frozen working fluid.

Numerous starts from the frozen state demonstrated consistent restart behavior. A preheated condenser initially accelerated startup but did not affect the steady-state condition or the time required to achieve it. The robustness predicted by the frozen startup limit calculation was confirmed with experimental results.

Objective 2 : Flight and Ground Performance Comparison

The second objective was comparison of microgravity performance with ground test performance. The experimental results indicate homogeneous and arterial wick heat pipe performances were insensitive to gravity effects. For these heat pipes, microgravity performance closely matched ground thermal vacuum performance, including startup transient and steady-state behavior. The discrepancies between the ground and flight data for the annular gap wick heat pipe are unresolved. Further investigation is required for the determination of any potential differences between terrestrial and microgravity performance.

Objective 3 : Design Assessment

The third objective was performance assessment of three heat pipe designs. Each of the three designs had unique strengths. The homogeneous wick heat pipe had a smaller thermal resistance, the annular gap wick heat pipe started more quickly, and the arterial wick heat pipe had a larger performance margin.

Thermal resistance decreased for all three heat pipes as the heat transfer rate and effective condenser length increased. The thermal resistances of the homogeneous, annular gap, and arterial wick designs were 0.38, 0.55, and 0.42 °C/W at a maximum transmitted power of 225 W to 235 W. The annular gap wick heat pipe had a notably higher resistance initially due to significant working fluid overcharge.

Steady-state operation was consistent with theory and the three heat pipes performed within the predicted performance envelopes. The homogeneous and annular

gap wick designs operated near the viscous and sonic limits at low temperatures. The arterial wick heat pipe demonstrated the largest performance margin.

All three heat pipes are robust designs. Differences in startup speed and thermal resistance are not as significant as the difference in performance margins. For this reason, the arterial wick heat pipe is judged to have a slight advantage over the other heat pipe designs.

Recommendations

The experimental data and results of this study are available for validation of liquid metal heat pipe startup transient models. Validation and improvement of these critical tools will assist in the design of future systems. Accurate performance predictions of liquid metal heat pipe startup behavior are required to build reliable and efficient thermal control systems for high temperature space applications.

The ground thermal vacuum test should be repeated for the annular gap wick heat pipe. A repeated test will help resolve the discrepancies between the current ground and flight data. Results of this test would determine the direction of future liquid metal heat pipe microgravity experiments. If microgravity experiments are continued, two conditions should be considered for further investigation: operation throughout a larger power range and increased thermal coupling between the condenser and surroundings. The first condition allows investigation of a larger portion of the performance envelope. The second condition could maintain frozen working fluid in the condenser and lead to better examination of startup difficulties.

A repeat of the thermal proof tests at Los Alamos National Laboratory would identify any performance changes since the heat pipes were manufactured in 1993. These tests could also verify that the effective condenser length of the arterial wick heat pipe is not limited by noncondensible gas or other phenomenon.

Summary

The three experimental objectives were successfully achieved. The series of startup tests characterized the behavior of the heat pipes during startup from the frozen state. Flight performance compared favorably with ground thermal vacuum test results. All the heat pipes demonstrated robustness and operated within the predicted performance envelopes. These results will serve as a benchmark for further liquid metal heat pipe studies and space system applications.

Appendix A: Design Specifications

Table 1 : Design Specifications

Design Properties	Units	Heat Pipe Wick Structure Design		
		Homogeneous	**Annular Gap**	**Arterial**
Container		Type 304 SS	Type 304 SS	Type 304 SS
Length, Overall	m	$6.10 \cdot 10^{-1}$	$6.10 \cdot 10^{-1}$	$6.10 \cdot 10^{-1}$
Length, Evaporator	m	$8.90 \cdot 10^{-2}$	$8.90 \cdot 10^{-2}$	$8.90 \cdot 10^{-2}$
Length, Adiabatic	m	NA	NA	NA
Length, Condenser	m	$5.21 \cdot 10^{-1}$	$5.21 \cdot 10^{-1}$	$5.21 \cdot 10^{-1}$
Outer Diameter	m	$2.30 \cdot 10^{-2}$	$2.30 \cdot 10^{-2}$	$2.30 \cdot 10^{-2}$
Wall Thickness	m	$8.9 \cdot 10^{-4}$	$8.9 \cdot 10^{-4}$	$8.9 \cdot 10^{-4}$
Wick Structure		Type 304 SS	Type 304 SS	Type 304 SS
Mesh Size		100	250	250
Wire Diameter	m	$1.20 \cdot 10^{-4}$	$0.40 \cdot 10^{-4}$	$0.40 \cdot 10^{-4}$
Pore Radius, Effective	m	$1.30 \cdot 10^{-4}$	$0.50 \cdot 10^{-4}$	$0.50 \cdot 10^{-4}$
Pore Radius, Hydraulic	m	$6.70 \cdot 10^{-5}$	$3.08 \cdot 10^{-5}$	$3.08 \cdot 10^{-5}$
Surface Porosity		0.5	0.6	0.6
Number of Mesh Layers		11	4	4
Wick Thickness	m	$2.3 \cdot 10^{-3}$	$0.30 \cdot 10^{-3}$	$0.30 \cdot 10^{-3}$
Annular Gap / Artery Dia	m	NA	$1.00 \cdot 10^{-3}$	$1.00 \cdot 10^{-3}$
Vapor Diameter	m	$1.67 \cdot 10^{-2}$	$1.96 \cdot 10^{-2}$	$2.06 \cdot 10^{-2}$
Vapor Area	m^2	$2.19 \cdot 10^{-4}$	$3.02 \cdot 10^{-4}$	$3.32 \cdot 10^{-4}$
Liquid Permeability	m^2	$1.76 \cdot 10^{-10}$	$2.08 \cdot 10^{-8}$	$3.13 \cdot 10^{-8}$
Liquid Flow Area	m^2	$1.35 \cdot 10^{-4}$	$3.26 \cdot 10^{-5}$	$1.57 \cdot 10^{-6}$
Working Fluid		Potassium	Potassium	Potassium
Mass, Design	gram	44.0	42.7	17.3
Mass, Actual	gram	46.0	61.5	19.2
Mass, Overcharge		4.5%	44.0%	11.0%

Source: Woloshun & Sena (28)

Appendix B: Material Physical Properties

Table 2 : Material Physical Properties

Material Properties	Units	Temperature (Kelvin)				
		400	450	500	550	600
Type 304 Stainless Steel						
Density	kg / m^3	7900	7900	7900	7900	7900
Thermal Conductivity	W / m K	16.6	17.4	18.2	19.0	19.8
Specific Heat	J / kg K	515.0	525.5	536.0	546.5	557.0
Wick Structure						
Thermal Conductivity						
Homogeneous Wick	W / m K	29.23	29.29	29.33	29.34	29.32
Annular Gap Wick	W / m K	32.37	32.22	32.04	31.83	31.59
Arterial Wick	W / m K	32.37	32.22	32.04	31.83	31.59
Friction Factor, Liquid						
Homogeneous Wick	N / m^3 W	9.65	8.47	7.52	6.76	6.16
Annular Gap Wick	N / m^3 W	0.34	0.30	0.26	0.24	0.21
Arterial Wick	N / m^3 W	4.66	4.09	3.63	3.26	2.97
Friction Factor, Vapor						
Homogeneous Wick	N / m^3 W	10336	882.8	113.02	20.38	4.88
Annular Gap Wick	N / m^3 W	5427	463.6	59.35	10.70	2.56
Arterial Wick	N / m^3 W	4486	383.2	49.06	8.85	2.12
Potassium						
Sat Vapor Pressure	N / m^2	$2.17 \cdot 10^{-2}$	$3.11 \cdot 10^{-1}$	$2.91 \cdot 10^{0}$	$1.90 \cdot 10^{+1}$	$9.20 \cdot 10^{+1}$
Density, Liquid	kg / m^3	814.1	801.9	789.9	778.2	766.5
Density, Vapor	kg / m^3	$2.16 \cdot 10^{-7}$	$3.36 \cdot 10^{-6}$	$2.95 \cdot 10^{-5}$	$1.71 \cdot 10^{-4}$	$7.33 \cdot 10^{-4}$
Kin Viscosity, Liquid	m^2 / s	$5.02 \cdot 10^{-7}$	$4.38 \cdot 10^{-7}$	$3.86 \cdot 10^{-7}$	$3.44 \cdot 10^{-7}$	$3.11 \cdot 10^{-7}$
Kin Viscosity, Vapor	m^2 / s	$4.33 \cdot 10^{+1}$	$3.68 \cdot 10^{0}$	$4.67 \cdot 10^{-1}$	$8.36 \cdot 10^{-2}$	$1.99 \cdot 10^{-2}$
Dyn Viscosity, Liquid	kg / m s	$4.09 \cdot 10^{-4}$	$3.51 \cdot 10^{-4}$	$3.05 \cdot 10^{-4}$	$2.68 \cdot 10^{-4}$	$2.38 \cdot 10^{-4}$
Dyn Viscosity, Vapor	kg / m s	$9.35 \cdot 10^{-6}$	$1.23 \cdot 10^{-5}$	$1.38 \cdot 10^{-5}$	$1.43 \cdot 10^{-5}$	$1.46 \cdot 10^{-5}$
Surface Tension Coef	N / m	$1.05 \cdot 10^{-1}$	$1.02 \cdot 10^{-1}$	$9.83 \cdot 10^{-2}$	$9.50 \cdot 10^{-2}$	$9.17 \cdot 10^{-2}$
Heat of Vaporization	J / kg	$2.20 \cdot 10^{+6}$	$2.18 \cdot 10^{+6}$	$2.17 \cdot 10^{+6}$	$2.15 \cdot 10^{+6}$	$2.13 \cdot 10^{+6}$
Thermal Conductivity	W / m K	48.0	46.6	45.2	43.8	42.3
Const P Specific Heat	J / kg K	531.9	609.5	669.8	742.0	819.4
Const V Specific Heat	J / kg K	319.2	386.8	437.6	496.6	557.6

Table 2 (continued) : Material Physical Properties

Material Properties	Units	Temperature (Kelvin)			
		650	700	750	800
Type 304 Stainless Steel					
Density	kg / m^3	7900	7900	7900	7900
Thermal Conductivity	W / m K	20.5	21.2	21.9	22.6
Specific Heat	J / kg K	563.3	569.5	575.8	582.0
Wick Structure					
Thermal Conductivity					
Homogeneous Wick	W / m K	29.23	29.11	28.98	28.82
Annular Gap Wick	W / m K	31.28	30.95	30.60	30.22
Arterial Wick	W / m K	31.28	30.95	30.60	30.22
Friction Factor, Liquid					
Homogeneous Wick	N / m^3 W	5.70	5.34	5.07	4.86
Annular Gap Wick	N / m^3 W	0.20	0.19	0.18	0.17
Arterial Wick	N / m^3 W	2.75	2.58	2.45	2.35
Friction Factor, Vapor					
Homogeneous Wick	N / m^3 W	1.48	0.54	0.23	0.11
Annular Gap Wick	N / m^3 W	0.78	0.29	0.12	0.06
Arterial Wick	N / m^3 W	0.64	0.24	0.10	0.05
Potassium					
Sat Vapor Pressure	N / m^2	$3.47 \cdot 10^{+2}$	$1.07 \cdot 10^{+3}$	$2.78 \cdot 10^{+3}$	$6.34 \cdot 10^{+3}$
Density, Liquid	kg / m^3	754.9	743.3	731.7	719.9
Density, Vapor	kg / m^3	$2.49 \cdot 10^{-3}$	$7.03 \cdot 10^{-3}$	$1.72 \cdot 10^{-2}$	$3.74 \cdot 10^{-2}$
Kin Viscosity, Liquid	m^2 / s	$2.85 \cdot 10^{-7}$	$2.64 \cdot 10^{-7}$	$2.48 \cdot 10^{-7}$	$2.35 \cdot 10^{-7}$
Kin Viscosity, Vapor	m^2 / s	$5.96 \cdot 10^{-3}$	$2.17 \cdot 10^{-3}$	$9.23 \cdot 10^{-4}$	$4.45 \cdot 10^{-4}$
Dyn Viscosity, Liquid	kg / m s	$2.15 \cdot 10^{-4}$	$1.96 \cdot 10^{-4}$	$1.81 \cdot 10^{-4}$	$1.69 \cdot 10^{-4}$
Dyn Viscosity, Vapor	kg / m s	$1.48 \cdot 10^{-5}$	$1.52 \cdot 10^{-5}$	$1.59 \cdot 10^{-5}$	$1.66 \cdot 10^{-5}$
Surface Tension Coef	N / m	$8.84 \cdot 10^{-2}$	$8.51 \cdot 10^{-2}$	$8.18 \cdot 10^{-2}$	$7.85 \cdot 10^{-2}$
Heat of Vaporization	J / kg	$2.11 \cdot 10^{+6}$	$2.09 \cdot 10^{+6}$	$2.07 \cdot 10^{+6}$	$2.04 \cdot 10^{+6}$
Thermal Conductivity	W / m K	40.9	39.4	38.0	36.5
Const P Specific Heat	J / kg K	895.3	964.6	1022.0	1066.0
Const V Specific Heat	J / kg K	615.0	664.5	703.0	729.0

Sources: Faghri (6), Brennan and Kroliczek (36), Incropera and DeWitt (42), and Vargaftik (45)

Appendix C: Fabrication Procedures

The following fabrication procedures were obtained from Los Alamos National Laboratory (29).

Stainless Steel Cleaning Procedure

1) Wash in Freon until grease is removed, typically 15 minutes.
2) Clean in ultrasonic cleaner for 5 minutes.
3) Soak in caustic cleaner solution for 15 minutes (11 parts water, 1 part sodium hydroxide, 1 part hydrogen peroxide); flush in hot tap water.
4) Repeat above step 3 times.
5) Rinse in hot water.
6) Rinse in distilled water.
7) Clean in ultrasonic cleaner for 5 minutes.
8) Rinse in ethanol.
9) Clean in ultrasonic cleaner for 5 minutes.
10) Vacuum degas at 600 °C for 30 min

Container & Wick Fabrication

1) Draw down copper tube to form wick mandrel; for arterial wick, machine two circular bottom grooves in the mandrel to form the arteries.
2) Cut wire mesh to size; clean according to above procedure.
3) Wrap screen around copper mandrel; tack weld after each revolution.
4) Insert screen and mandrel into stainless steel tube.

5) Draw down assembly to achieve 20% compression of the screen and cut to heat pipe length.

6) Dissolve copper mandrel and remove wick.

7) Sinter wick and return to container.

8) Fabricate stainless steel end plugs and fill stem; clean these components.

9) TIG weld fill stem to end plug and weld end plugs to container.

10) Helium leak check the assembly.

11) Vacuum degas at 600 °C for 30 min prior to filling.

12) Distill potassium into heat pipe according to procedure below.

13) Wet in heat pipe and characterize by heating to 500 °C for 40 hours.

14) Form frozen plug of potassium in fill stem, between heat pipe end cap and valve.

15) In a vacuum glove box, cut fill stem, remove valve and TIG weld a cap to the fill stem.

Potassium Charge

Fill Known Volume Pot

1) Attach input line of source container to argon pressure line; attach output line to known volume pot connected to vacuum line.

2) Pressurize container at 10-12 psig with argon.

3) Heat source container to 200 °C (melt temperature of potassium is 64 °C).

4) Open vacuum line to allow pressurized liquid potassium to fill the known volume pot.

5) Close pressure lines and turn off heaters.

6) Remove known volume pot and cool.

Fill Distillation Pot

1) Attach input line of known volume pot to argon pressure line; attach output line to distillation pot.

2) Connect distillation pot and heat pipe with a vacuum / argon pressure line to form distillation apparatus as shown in Figure 21.

3) Pressurize known volume pot at 10-12 psig with argon; evacuate line between distillation pot and heat pipe.

4) Heat known volume and distillation pots; melt potassium in volume pot.

5) Open vacuum line to allow pressurized liquid potassium to fill the distillation pot.

6) Close pressure lines and turn off heaters.

7) Remove known volume pot and cap off distillation pot input line; leave distillation pot attached to vacuum / argon pressure line.

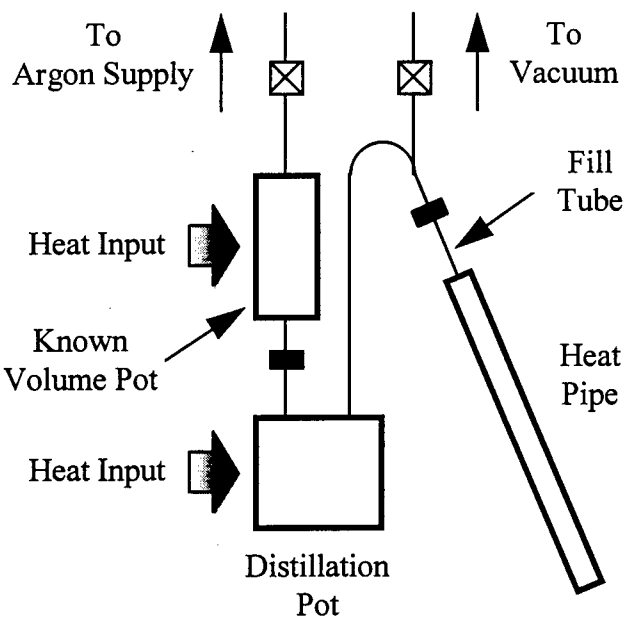

Figure 21 : Distillation Apparatus

Distill Potassium Into Heat Pipe

1) Evacuate pressure line between distillation pot and heat pipe to 10^{-5} torr; leave vacuum line open and pump active.

2) Preheat distillation pot, vacuum line, and heat pipe to 150 °C.

3) Heat distillation pot to 450 °C; this temperature creates a pressure of 10 torr in distillation pot.

4) Fill heat pipe; pressure differential causes liquid potassium to flow into heat pipe.

5) Cool to allow potassium to solidify.

6) Close vacuum line and remove distillation pot.

7) Turn heat pipe upside down and place chill block at union of vacuum line and heat pipe fill stem.

8) Heat the heat pipe to melt potassium; chill block will solidify potassium to form a plug at the union.

9) Disconnect vacuum line and attach valve to heat pipe fill stem.

Appendix D: Thermocouple Locations

Table 3 : Thermocouple Locations

Thermocouple Number	Heat Pipe Location	Distance From Evap End Cap (cm)
1,2	Evaporator Heater	1.3
3,4	Evaporator Heater	3.8
5	Condenser	13.3
6	Condenser	15.9
7	Condenser	18.4
8	Condenser	21.0
9	Condenser	23.5
10	Condenser	26.0
11	Condenser	28.6
12	Condenser	31.1
13	Condenser	33.7
14	Condenser	36.2
15	Condenser	38.7
16	Condenser	41.3
17	Condenser	43.8
18	Condenser	46.4
19	Condenser	48.9
20	Condenser	51.4
21,22	Condenser Heater	57.8
23,24	Condenser Heater	60.3

Source: Phillips Laboratory (37)

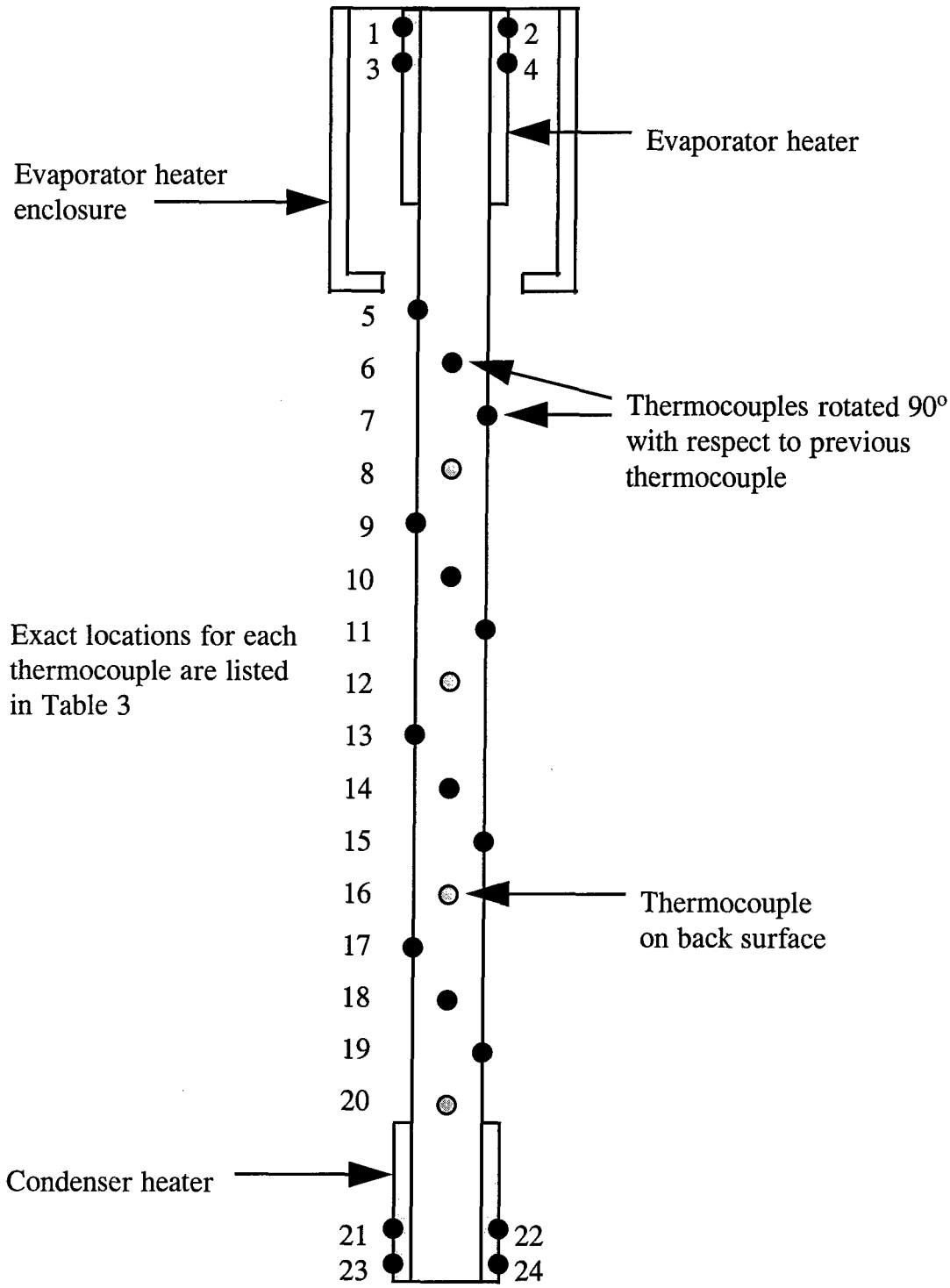

Figure 22 : Thermocouple Positions

Bibliography

1. Woloshun, Keith A. and others. "High Temperature Heat Pipe Experiments in Low Earth Orbit," 1993 National Heat Transfer Conference, Paper 93-HT-23 (8-11 August 1993). New York: American Society of Mechanical Engineers, 1993.

2. Critchley, Eric P. and Mary E. Corrigan. "Design of a Liquid Metal Heat Pipe Space Experiment," 12th Symposium on Space Nuclear Power and Propulsion (8-12 January 1995). New York: American Institute of Physics, 1995.

3. Phillips Laboratory, Air Force Materiel Command. Liquid Metal Thermal Experiment Point Paper. Kirtland AFB NM, 4 September 1996.

4. Peterson, G. P. An Introduction to Heat Pipes: Modeling, Testing and Applications. New York: John Wiley & Sons, Incorporated, 1994.

5. Dunn, P. D. and D. A. Reay. Heat Pipes (Fourth Edition). Tarrytown NY: Elsevier Science Incorporated, 1994.

6. Faghri, Amir. Heat Pipe Science and Technology. Washington: Taylor & Francis, 1995.

7. Brennan, Patrick J. and Edward J. Kroliczek. Heat Pipe Design Handbook, Volume I. Towson MD: B & K Engineering, Incorporated, June 1979.

8. Merrigan, Michael A. Technical Staff Member, RRA Incorporated, Los Alamos NM. Personal interview. 7 August 1996.

9. Dean, Virginia F. and others. Heat Pipe Space Nuclear Reactor Design Assessment: Volume I of II, Design Status of the SP-100 Heat Pipe Space Nuclear Reactor System. AFW-TR-84-126, Vol I. Kirtland AFB NM: Air Force Weapons Laboratory, August 1985 (AD-A160279).

10. Tournier, Jean-Michel P. and Mohamed S. El-Genk. HPTAM, A Two-Dimensional Heat Pipe Transient Analysis Model, Including the Startup From a Frozen State. NASA Lewis Research Center Grant Number NAG3-941, Final Report Number UNM-ISNPS-2-1996. Albuquerque NM: Institute for Space and Nuclear Power, University of New Mexico, College of Engineering, May 1996.

11. Chi, S. W. Heat Pipe Theory and Practice. Washington: Hemisphere Publishing Corporation, 1976.

12. Silverstein, Calvin C. Design and Technology of Heat Pipes for Cooling and Heat Exchange. Washington: Hemisphere Publishing Corporation, 1992.

13. Brennan, Patrick J. and others. "Flight Data for the Cryogenic Heat Pipe CRYOHP) Experiment," AIAA 28th Thermophysics Conference (AIAA Paper #93-2735). Washington DC: American Institute of Aeronautics and Astronautics, 1993.

14. Brennan, Patrick J. and others. "Design and Performance of the Cryogenic Two Phase Flight Experiment (CRYOTP)," 24th International Conference on Environmental Systems and 5th European Symposium on Space Environmental Control Systems (SAE Paper #941474). Warrendale PA: SAE International, 1994.

15. Alario, Joseph P. "Monogroove Heat Pipe Radiator Shuttle Flight Experiment: Design, Analysis and Testing," SAE Technical Paper Series #840950: 1-7 (1984).

16. Buchko, Matthew T. and others. "Flight and Ground Test Data Analysis for the Heat Pipe Performance (HPP) Experiment," 24th International Conference on Environmental Systems and 5th European Symposium on Space Environmental Control Systems (SAE Paper #941300). Warrendale PA: SAE International, 1994.

17. Yun, Seokgeun "James" and others. "Design and Ambient Testing of the Flight Starter Cold Plate," SAE Technical Paper Series #840950: 1-10 (1984).

18. Hall, M. L. Numerical Modeling of the Transient Thermohydraulic Behavior of High-Temperature Heat Pipes for Space Reactor Applications. PhD dissertation. North Carolina State University, Raleigh NC, 1988.

19. Hall, M. L., M. A. Merrigan, and R. S. Reid. "Status Report of the THROHPUT Transient Heat Pipe Modeling Code," Proceedings of the 11th Symposium on Space Nuclear Power and Propulsion (9-13 January 1994). Albuquerque NM: Institute for Space Nuclear Power Studies, 1994.

20. Tournier, Jean-Michel and Mohamed S. El-Genk. "Transient Analysis of the Startup of a Sodium Heat Pipe From a Frozen State," American Institute of Physics Conference Proceedings (9 January 1996). New York: American Institute of Physics, 1996.

21. Kemme, J. E. "Heat Pipe Capability Experiments." Los Alamos Scientific Laboratory Report LA-3585-MS. Los Alamos National Laboratory, Los Alamos NM. October 1966.

22. Deverall, J. E., J. E. Kemme and L. W. Florschuetz. "Sonic Limitations and Startup Problems of Heat Pipes." Los Alamos Scientific Laboratory Report LA-4518. Los Alamos National Laboratory, Los Alamos NM. November 1970.

23. Kemme, J. E., E. S. Keddy, and J. R. Phillips. "Performance Investigations of Liquid Metal Heat Pipes for Space and Terrestrial Applications," Proceedings of the 3rd International Heat Pipe Conference. 260-267. New York: American Institute of Aeronautics and Astronautics, 1978.

24. Merrigan, M. A., E. S. Keddy, and J. T. Sena. "Transient Performance Investigation of a Space Power System Heat Pipe," AIAA / ASME 4th Joint Thermophysics and Heat Transfer Conference (2-4 June 1986). New York: American Institute of Aeronautics and Astronautics, 1986.

25. Woloshun, K. A. and others. "Radial Heat Flux Limits in Potassium Heat Pipes: An Experimental and Analytical Investigation," Proceedings of the 7th Symposium on Space Nuclear Power Systems (7-11 January 1990). Albuquerque NM: Institute for Space Nuclear Power Studies, 1990.

26. Camarda, C. J. Analysis and Radiant Heating Tests of a Heat Pipe Cooled Leading Edge. NASA Report TN-8468. Hampton VA: NASA Langley Research Center, August 1977.

27. "Preliminary Heat Pipe Testing Program: Final Technical Report." Report to U. S. Department of Energy, San Francisco Operations Office, San Francisco CA. March 1981.

28. Los Alamos National Laboratory. Heat Pipe Final Designs. Los Alamos NM, April 1992.

29. Los Alamos National Laboratory. Heat Pipe Fabrication Procedures. Los Alamos NM, June 1992.

30. Phillips Laboratory, Air Force Materiel Command. Liquid Metal Thermal Experiment Phase III Flight Safety Data Package. Kirtland AFB NM, December 1995.

31. Phillips Laboratory, Air Force Materiel Command. Memorandum for Record regarding Thermal Proof Test of Liquid Metal Thermal Experiment. Kirtland AFB NM, 11 August 1995.

32. Cao, Y. and A. Faghri. "Closed-Form Analytical Solutions of High-Temperature Heat Pipe Startup and Frozen Startup Limitation," Journal of Heat Transfer, 114: 1028-1035 (November 1992).

33. Woloshun, K. A., M. A. Merrigan, and E. D. Best. HTPIPE: A Steady-State Heat Pipe Analysis Program, A User's Manual. LA-11324-M. Los Alamos NM: Los Alamos National Laboratory, November 1988.

34. Tournier, Jean-Michel and Mohamed S. El-Genk. "An Analysis of the Startup of a Radiatively-Cooled Sodium Heat Pipe From a Frozen State," AIChE Symposium Series-Heat Transfer, 1996 National Heat Transfer Conference, Vol 92, Number 310 (3-5 August 1996). New York: American Institute of Physics, 1996.

35. Ivanovskii, M. N., V. P. Sorokin, and I. V. Yagodkin. The Physical Principles of Heat Pipes. New York: Oxford University Press, 1982.

36. Brennan, Patrick J. and Edward J. Kroliczek. Heat Pipe Design Handbook, Volume II. Towson MD: B & K Engineering, Incorporated, June 1979.

37. Phillips Laboratory, Air Force Materiel Command. Liquid Metal Thermal Experiment Thermal Vacuum Test Plan. Kirtland AFB NM, 31 August 1995.

38. Jang, J. H. and others. "Mathematical Modeling and Analysis of Heat Pipe Startup From the Frozen State," Journal of Heat Transfer, 112: 586-594 (August 1990).

39. Keddy, Michael D., Michael A. Merrigan, and Eric Critchley. "Modeling the Mass Migration Phenomena in Partially Frozen Heat Pipes," Proceedings of the 11th Symposium on Space Nuclear Power and Propulsion (9-13 January 1994). Albuquerque NM: Institute for Space Nuclear Power Studies, 1994.

40. Jang, J. H. "A Study of Startup Characteristics of a Potassium Heat Pipe from the Frozen State," Journal of Thermophysics and Heat Transfer, 9: 117-122 (1995).

41. Woloshun, Keith A. Thermal Engineering Team Leader, Los Alamos National Laboratory, Los Alamos NM. Personal interview. 8 August 1996.

42. Incropera, Frank P. and David P. DeWitt. Fundamentals of Heat and Mass Transfer (Third Edition). New York: John Wiley & Sons, Incorporated, 1990.

43. Gurule, Anthony P. "Liquid Metal Test Experiment: Computer Thermal Analysis." Report to Phillips Laboratory, Kirtland AFB NM. June 1995.

44. Sena, J. Tom. Technical Staff Member, Los Alamos National Laboratory, Los Alamos NM. Personal interview. 8 August 1996.

45. Vargaftik, N. B. Tables on the Thermophysical Properties of Liquids and Gases (Second Edition). Washington: Hemisphere Publishing Corporation, 1975.

Vita

Capt Timothy J. Dickinson [redacted]. He graduated from Eureka High School in 1986 and entered undergraduate studies and the Air Force Reserve Officer Training Corps at the University of Missouri - Rolla. In December 1990, he graduated with a Bachelor of Science degree in Aerospace Engineering and received his commission.

In September 1991, he entered active duty and was assigned to Los Angeles AFB. He served as an engineering acquisition officer in the Titan and Global Positioning System Program Offices. He also conducted a composite materials research program during an engineering internship with the Aerospace Corporation. In June 1995, he began his second assignment at the Air Force Institute of Technology, Wright-Patterson AFB. He entered the School of Engineering and earned a Master of Science degree in Aeronautical Engineering. Upon graduation in December 1996, he was assigned to U. S. Strategic Command Headquarters at Offutt AFB.

[redacted]

REPORT DOCUMENTATION PAGE

Form Approved
OMB No. 0704-0188

1. AGENCY USE ONLY (Leave blank)	2. REPORT DATE	3. REPORT TYPE AND DATES COVERED
	December 1996	Master's Thesis

4. TITLE AND SUBTITLE
PERFORMANCE ANALYSIS OF A LIQUID METAL HEAT PIPE SPACE SHUTTLE EXPERIMENT

5. FUNDING NUMBERS

6. AUTHOR(S)
Timothy J. Dickinson, Captain, USAF

7. PERFORMING ORGANIZATION NAME(S) AND ADDRESS(ES)
Air Force Institute of Technology
2950 P Street
WPAFB OH 45433-7765

8. PERFORMING ORGANIZATION REPORT NUMBER
AFIT/GAE/ENY/96D-2

9. SPONSORING / MONITORING AGENCY NAME(S) AND ADDRESS(ES)
PL/VTPT
3550 Aberdeen Avenue SE
Building 30117
Kirtland AFB NM 87117-5776

10. SPONSORING / MONITORING AGENCY REPORT NUMBER

11. SUPPLEMENTARY NOTES

12a. DISTRIBUTION / AVAILABILITY STATEMENT
Approved for public release; distribution unlimited

12b. DISTRIBUTION CODE
A

13. ABSTRACT *(Maximum 200 words)*

Future spacecraft technologies require advanced high-temperature thermal control systems. Liquid metal heat pipes are ideally suited for such applications. However, their behavior during microgravity operation is not yet understood. This study investigated liquid metal heat pipe performance in such an environment. Three stainless steel / potassium heat pipes were flown on space shuttle mission STS-77 in May 1996. The objectives of the experiment were characterization of the frozen startup and restart transients, comparison of flight and ground test data, and assessment of three different heat pipe designs. Heat pipe performance was characterized prior to the flight experiment. Predicted performance envelopes for each heat pipe were determined from theoretical calculations. Performance baselines were established from ground thermal vacuum test results. These pre-flight results were compared with those from the flight experiment. Thermal resistances were calculated for each heat pipe design. Microgravity operation did not adversely impact the startup or restart behavior of the heat pipes. The heat pipes operated within the predicted performance envelopes. The three designs had distinct startup characteristics yet similar steady-state performance. These results will serve as a benchmark for further liquid metal heat pipe studies and space system applications.

14. SUBJECT TERMS	15. NUMBER OF PAGES
Heat Pipe, Liquid Metal, Space Experiment, Thermal Energy Transport, Heat Transfer	90
	16. PRICE CODE

17. SECURITY CLASSIFICATION OF REPORT	18. SECURITY CLASSIFICATION OF THIS PAGE	19. SECURITY CLASSIFICATION OF ABSTRACT	20. LIMITATION OF ABSTRACT
Unclassified	Unclassified	Unclassified	UL